Research Paper

THEMED ISSUE: Seismotectonics of the San Andreas Fault System in the San Gorgonio Pass Region

GEOSPHERE

GEOSPHERE, v. 16, no. 3

https://doi.org/10.1130/GES02160.1

14 figures; 1 table

CORRESPONDENCE: spotila@vt.edu

CITATION: Spotila, J.A., Mason, C.C., Valentino, J.D., and Cochran, W.J., 2020, Constraints on rock uplift in the eastern Transverse Ranges and northern Peninsular Ranges and implications for kinematics of the San Andreas fault in the Coachella Valley, California, USA: Geosphere, v. 16, no. 3, p. 723–750, https://doi.org/10.1130/GES02160.1.

Science Editor: Andrea Hampel
Guest Associate Editor: Michele L. Cooke

Received 29 May 2019
Revision received 1 November 2019
Accepted 13 February 2020

Published online 19 March 2020

Constraints on rock uplift in the eastern Transverse Ranges and northern Peninsular Ranges and implications for kinematics of the San Andreas fault in the Coachella Valley, California, USA

James A. Spotila[1,*], Cody C. Mason[2,*], Joshua D. Valentino[3,*], and William J. Cochran[4,*]

[1]Department of Geosciences, Virginia Tech, 4044 Derring Hall, Blacksburg, Virginia 24061, USA
[2]Department of Geosciences, University of West Georgia, Callaway Building, 1601 Maple Street, Carrollton, Georgia 30118, USA
[3]GeoConcepts Engineering, Inc., 19955 Highland Vista Drive, Suite 170, Ashburn, Virginia 20147, USA
[4]Fugro, 101 West Main Street, Suite 350, Norfolk, Virginia 23504, USA

ABSTRACT

The nexus of plate-boundary deformation at the northern end of the Coachella Valley in southern California (USA) is complex on multiple levels, including rupture dynamics, slip transfer, and three-dimensional strain partitioning on nonvertical faults (including the San Andreas fault). We quantify uplift of mountain blocks in this region using geomorphology and low-temperature thermochronometry to constrain the role of long-term vertical deformation in this tectonic system. New apatite (U-Th)/He (AHe) ages confirm that the rugged San Jacinto Mountains (SJM) do not exhibit a record of rapid Neogene exhumation. In contrast, in the Little San Bernardino Mountains (LSBM), rapid exhumation over the past 5 m.y. is apparent beneath a tilted AHe partial retention zone, based on new and previously published data. Both ranges tilt away from the Coachella Valley and have experienced minimal denudation from their upper surface, based on preservation of weathered granitic erosion surfaces. We interpret rapid exhumation at 5 Ma and the gentle tilt of the erosion surface and AHe isochrons in the LSBM to have resulted from rift shoulder uplift associated with extension prior to onset of transpression in the Coachella Valley. We hypothesize that the SJM have experienced similar rift shoulder uplift, but an additional mechanism must be called upon to explain the pinnacle-like form, rugged escarpment, and topographic disequilibrium of the northernmost SJM massif. We propose that this form stems from erosional resistance of the Peninsular Ranges batholith relative to more-erodible foliated metamorphic rocks that wrap around it. Our interpretations suggest that neither the LSBM nor SJM have been significantly uplifted under the present transpressive configuration of the San Andreas fault system, but instead represent relict highs due to previous tectonic and erosional forcing.

INTRODUCTION

As the deformation history of the Earth's best-studied plate boundaries grows more thoroughly defined, our understanding of tectonic processes advances toward a functional description of lithospheric behavior. The San Andreas fault (SAF) system, lying between the North America and Pacific plates, is one of the world's most thoroughly examined plate boundaries, yet still exhibits first-order features that have yet to be documented and explained. This is particularly true in southern California (USA), where the SAF system comprises broad complexity, including regional transpressive obliquity (Big Bend), a large restraining bend (San Gorgonio Pass), evolving partitioning with subparallel faults (San Jacinto fault and Eastern California shear zone), internal reorganization of fault strands, nonvertical strike-slip fault geometry, history of plate motion changes, and transition to the Gulf of California extensional province (Matti and Morton, 1993; Sieh et al., 1993; Atwater and Stock, 1998; Axen and Fletcher, 1998; Spotila et al., 1998; Yule and Sieh, 2003; Janecke et al., 2010; Fuis et al., 2017). Here we quantify geologic deformation associated with these phenomenological elements at their focal point in the Coachella Valley (Fig. 1).

An understudied realm of tectonics of the southern SAF system is mountain building and how it relates to plate boundary strain. Although well studied in and to the north of the San Bernardino Mountains (SBM) (Spotila et al., 2007), the kinematics and history of late Cenozoic uplift of mountain blocks bounding the Coachella Valley are not yet fully explained. Understanding rock uplift is particularly important in this region, given the role of partitioned pure shear associated with current transpressive and previous transtensional plate motion obliquity. For example, uplift patterns can be used specifically to test kinematic models of fault deformation (e.g., Cooke and Dair, 2011; Fattaruso et al., 2014, 2016). Despite previous work, the uplift history and kinematics of the largest ranges bounding the Coachella Valley, the Little San Bernardino Mountains (LSBM) to the east and the San Jacinto Mountains (SJM) to the west, are still not fully explained (Wolf et al., 1997; Sabala, 2010) (see below). Uplift patterns of these ranges have thus not yet been placed in context of the tectonic evolution of the Coachella Valley and the SAF system. For example, it is unknown whether these blocks were uplifted due to Neogene transpression or are remnants of earlier tectonic phases. As a

*E-mail: spotila@vt.edu; cmason@westga.edu; joshua.valentino@terracon.com; w.cochran@fugro.com

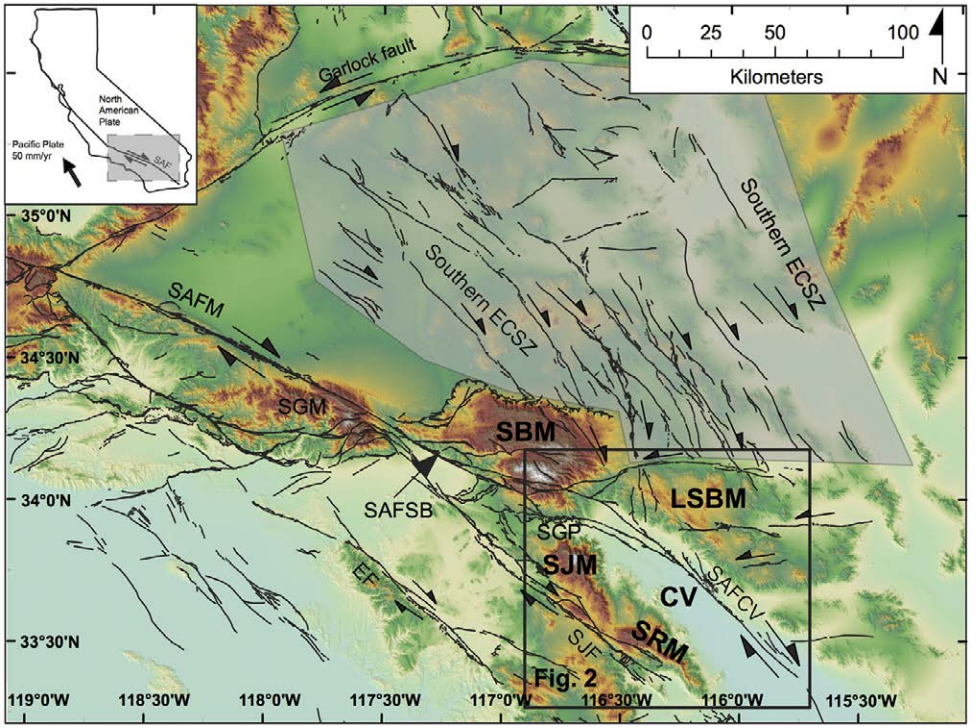

Figure 1. Tectonic map of the San Andreas fault (SAF) system in southern California, USA (location shown in inset). CV—Coachella Valley; ECSZ—Eastern California shear zone (shaded region); EF—Elsinore fault; LSBM—Little San Bernardino Mountains; SAFCV—Coachella Valley segment of SAF; SAFM—Mojave segment of SAF; SAFSB—San Bernardino segment of SAF; SBM—San Bernardino Mountains; SGM—San Gabriel Mountains; SGP—San Gorgonio Pass; SJF—San Jacinto fault; SJM—San Jacinto Mountains; SRM—Santa Rosa Mountains.

result, it is not clear in which context these mountains should be viewed in regard to the distribution of vertical deformation associated with the modern SAF system, unlike many other ranges to the north (Spotila et al., 2007).

In this study, we apply geomorphology and low-temperature thermochronometry to constrain the timing and magnitude of uplift of the LSBM and SJM. We synthesize topographic analysis, mapping of a deeply weathered erosion surface, and reconnaissance apatite (U-Th)/He (AHe) dating with existing data to document the pattern of rock uplift and denudation throughout these ranges. From these constraints, we draw new conclusions regarding the uplift kinematics of these ranges and propose implications for the tectonic evolution of the Coachella Valley.

TECTONIC BACKGROUND

Tectonic Evolution of the Coachella Valley

The Coachella Valley is a 75-km-long, 30-km-wide, northwest-trending valley with elevations near sea level that lies northwest of the Salton Sea (Fig. 2). The valley lies within the Salton Trough and is the northern, landward continuation of the Gulf of California rift system, although it is now cut by strands of the southern SAF system. The valley is enclosed by the rugged western escarpment of the LSBM to the northeast, the eastern escarpment of the SJM and Santa Rosa Mountains to the southwest, and the SBM to the northwest. Valley fill ranges in thickness from <2 km in the north to ~5 km in the south, and comprises late Miocene and younger nonmarine alluvial and fluvial-deltaic deposits with occasional marine incursions from the Gulf of California and sediment input from the Colorado River (Langenheim et al., 2005; Dorsey et al., 2011; Ajala et al., 2019). Individual parts of the Salton Trough exhibit syndepositional fault control and rapid subsidence beginning at ca. 8 Ma due to regional extension (Dorsey et al., 2011). Extension was accommodated via pull-apart basins within the SAF system as well as by the West Salton detachment fault in the Plio-Pleistocene (Axen and Fletcher, 1998; Dorsey et al., 2011; Dorsey and Langenheim, 2015; Mason et al., 2017). Many extensional structures shut off with the inception of the San Jacinto fault zone to the west at ca. 1.1–1.3 Ma (Matti and Morton, 1993; Janecke et al., 2010).

The active southern SAF runs through the Coachella Valley, exhibiting local transpressive deformation with obliquity of ~5°. The SAF exhibits a 15-km-wide bend at the northern end of the valley, where it follows a narrow passage between the SJM and SBM through San Gorgonio Pass (Yule and Sieh, 2003). This bend marks the inflection to the more transpressive San Bernardino strand of the SAF to the northwest of the Coachella Valley (~27° oblique to plate motion) (Spotila et al., 2007). The SAF bifurcates just southeast of San Gorgonio Pass into the Mission Creek fault and Banning fault, which in turn transition into a diffuse series of north-dipping dextral-reverse faults, including the Garnet Hill fault and San Gorgonio Pass fault zone, which have uplifted several crystalline blocks in concert with thrust faults farther north (Spotila et al., 1998, 2001; Yule and Sieh, 2003; Langenheim et al., 2005; Cooke and Dair, 2011; Gold et al., 2015). Strands of the southern SAF dip steeply to the northeast throughout the Coachella Valley, with the dip shallowing to 50°–60° below a kink at 6–9 km depth (Fuis et al., 2017). Individual fault strands integrate into flower structures that core the transpressional zones in the center of the valley (Mecca

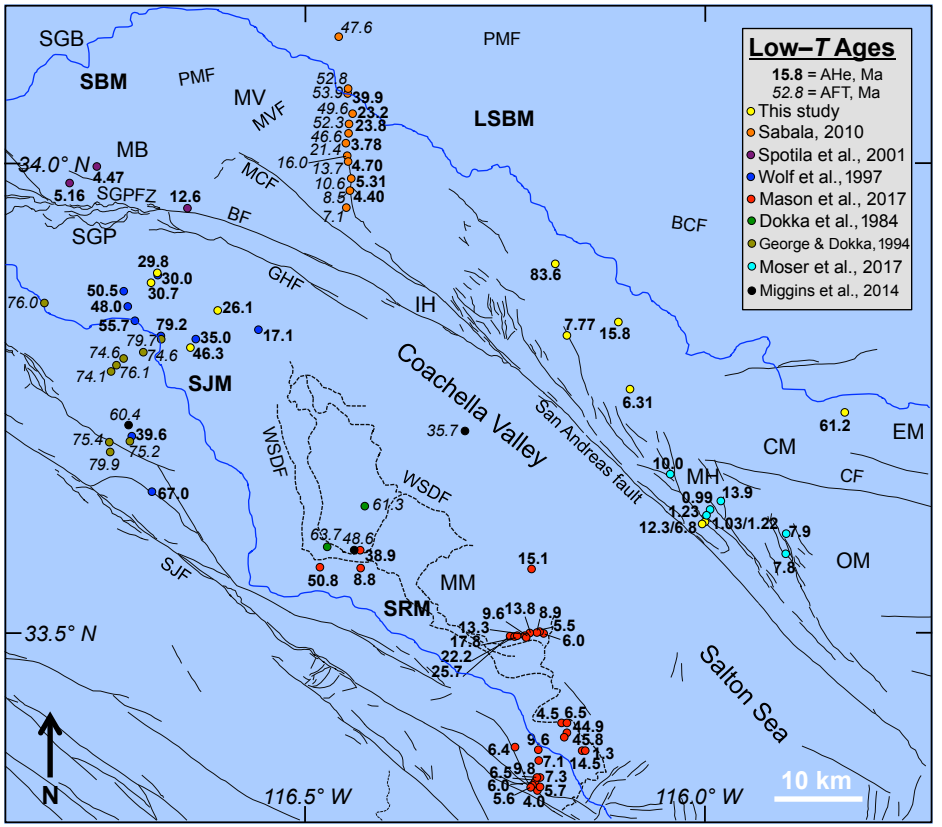

Figure 2. Map of the Coachella Valley showing published and new low-temperature (low-*T*) apatite (U-Th)/He (AHe) and apatite fission-track (AFT) thermochronometry ages. Blue line indicates the catchment boundary of the northern Coachella Valley. Ages from Moser et al. (2017) from the Mecca Hills are shown as averages (not calculated in the original study), in some cases with one outlier age dropped. The two ages we measured in the Mecca Hills are listed as doubles (e.g., 12.3/6.8), given that Moser et al. (2017) dated basically the same location (our age is listed first, Moser et al. [2017] age is given second). Note that some Sabala (2010) locations have both AHe and AFT ages. Locations shown are: CM—Cottonwood Mountains; EM—Eagle Mountains; IH—Indio Hills; LSBM—Little San Bernardino Mountains; MB—Morongo block; MH—Mecca Hills; MM—Martinez Mountain; MV—Morongo Valley; OM—Orocopia Mountains; SBM—San Bernardino Mountains; SGB—San Gorgonio block; SGP—San Gorgonio Pass; SJM—San Jacinto Mountains; SRM—Santa Rosa Mountains. Faults shown as solid black lines are: BCF—Blue Cut fault; BF—Banning fault; CF—Chiriaco fault; GHF—Garnet Hill fault; MCF—Mission Creek fault; MVF—Morongo Valley fault; PMF—Pinto Mountain fault; SJF—San Jacinto fault; SGPFZ—San Gorgonio Pass fault zone; WSDF (dashed)—West Salton detachment fault (WSDF after Axen and Fletcher, 1998).

and Indio Hills), where local Quaternary transpression has resulted in near-field deformation and basin inversion. Transpressional loading along the southern SAF also results in broad northeastward tilting (8°) of the central Salton block, which underlies the Coachella Valley basin and lies between the SAF and San Jacinto fault zone to the west (Dorsey and Langenheim, 2015).

The horizontal modern slip rate on the SAF in the Coachella Valley varies from 23 mm/yr in the south to 14–17 mm/yr in the northern Coachella Valley, representing ~30%–45% of relative plate motion (van der Woerd et al., 2006; Spinler et al., 2010; Behr et al., 2010). The remainder of plate motion is accommodated by the San Jacinto and Elsinore faults to the west and the Eastern California shear zone to the northeast (Thatcher et al., 2016). Although the southern SAF has been transpressional for the last few million years, it initiated when the Coachella Valley was experiencing extension and has likely been active in the valley for the past 6–5 m.y. (Matti and Morton, 1993; Powell, 1993).

History of Basement Blocks Bordering the Coachella Valley

The northern tip of the Coachella Valley terminates against the transpressively constructed SBM, which sit astride the northeastern margin of the SAF (Fig. 2). This range has been elevated as a series of basement blocks along convergent structures over the past 2–3 m.y. (Spotila et al., 1998). Structural style within the SBM farther from the SAF (~20–50 km) is dominated by low-angle thrusting that roots back to the point of convergence in San Gorgonio Pass and that results in broad plateau uplift (Spotila and Sieh, 2000). Within the near field of the SAF (<10 km), including within the strands of the fault zone itself, structural style is instead dominated by high-angle reverse faults that have uplifted narrow crustal slivers at high rates (Spotila et al., 2001). The kinematics of this uplift and exhumation pattern have been constrained using the deformation of a deeply weathered erosion surface (see below) as well as thermochronology. AHe ages in the near field of the SAF include Miocene (5–13 Ma) ages from the crystalline block just north of San Gorgonio Pass (the only ages from the SBM studies that fall within the area of Fig. 2) and <1 Ma ages from narrow crustal slivers directly along the SAF (Spotila et al., 1998, 2001). Cooling ages are generally older in the broad crystalline blocks at greater distances from the SAF. These define an AHe partial retention zone (PRZ) that was used as a passive marker to constrain the geometry of vertical deformation (Spotila et al., 1998; Blythe et al., 2000).

The SJM lie south of the SBM and San Gorgonio Pass and form the western flank of the

northern Coachella Valley (Fig. 2). This range is a part of the Peninsular Ranges batholith, which is an ~1100-km-long Jurassic to Cretaceous continental arc fragment in southern California and Baja California, Mexico (Silver and Chappell, 1988). The SJM exhibits extremely rugged northern and eastern slopes (maximum elevation of 3302 m), but is capped by a high-elevation plateau surface that slopes more gently downward to the range-bounding San Jacinto and Hot Springs faults to the west (see below) (Dibblee, 1981; Rossi, 2014; DiBiase et al., 2018). Despite steep slopes, the northern and eastern range fronts are not characteristic of actively faulted margins, leading to uncertainty regarding the kinematics and timing of SJM uplift (Dibblee, 1981) that has remained despite the addition of thermochronologic data. Wolf et al. (1997) measured mainly Paleogene AHe ages along a relief transect in the SJM that are consistent with the range of apatite fission-track (AFT) ages measured previously by Dokka (1984) and George and Dokka (1994) and subsequently by Miggins et al. (2014). These ages imply a history of rapid post-magmatic unroofing until the early Cenozoic, followed by much slower cooling and denudation (e.g., <60 °C since the early Tertiary; Miggins et al., 2014). The Wolf et al. (1997) ages define an ~7° west-tilted AHe PRZ, which roughly matches the westward basement tilt indicated by hornblende geobarometry (~15°) (Ague and Brandon, 1992). These ages do not, however, establish onset (or existence) of rapid exhumation of the SJM in the late Cenozoic. Previous work has therefore not resolved when or how the SJM block was uplifted due to Neogene tectonic motions, or whether instead the block is primarily a pre-SAF uplift that predates the modern tectonic setting. However, rapid erosion of the rugged northern and eastern faces of the SJM has at least been confirmed by several basinwide cosmogenic radionuclide erosion rates (overall range of 0.04–0.24 mm/yr) interpreted by Rossi (2014) for time scales of ~1–10 k.y.

The northeastern flank of the Coachella Valley is bounded by the LSBM (Fig. 2). This range bears many similarities to the SBM and consists mainly of Jurassic to Cretaceous granitic rocks related to the Sierra Nevada batholith and Proterozoic gneisses (Dibblee, 1982; Needy et al., 2009). The topography of the LSBM is more subdued than the SJM, with a maximum elevation of only 1775 m and without discrete uplifted blocks. The range also has an escarpment-like appearance, with a rugged slope that extends westward down to the SAF and an upper surface that has low relief and tapers gently eastward to merge with the high desert floor of the Mojave block. The only previous low-temperature thermochronometric data from the LSBM were obtained by Sabala (2010), who measured 12 AFT and 7 AHe ages in an ~1-km-relief transect along Long Canyon between the SAF and Pinto Mountain fault (Fig. 2). This study constrained age-elevation relationships spanning 7–54 Ma (AFT) and 4–40 Ma (AHe) that documented the late Cenozoic exhumation of the range. Forward and inverse modeling of these ages and AFT track-length distributions suggested slow cooling throughout much of the Cenozoic, with onset of rapid exhumation (0.4–0.6 mm/yr) in the past 5–7 m.y. (Sabala, 2010). The rapid Neogene exhumation was discernible only in samples within 12 km of the SAF and was interpreted to result from near-field transpressional deformation (e.g., rock uplift along a northeastward-dipping SAF). Sabala (2010) proposed that an unmapped northwest-trending fault formed the boundary between the young (west) and older (east) cooling ages, and that the older ages to the east form an AHe PRZ and AFT partial annealing zone that experienced unspecified magnitude of tilting to the north. Rapid erosion of the western escarpment is consistent with several cosmogenic radionuclide–based basinwide erosion rates (overall range of 0.05–0.48 mm/yr) interpreted by Rossi (2014) and rates of 0.2–0.4 mm/yr determined for the far northwestern LSBM and southeastern San Bernardino Mountains (Fosdick and Blisniuk, 2018).

The southern Coachella Valley is bound by several ranges and includes minor convergent zones within the valley just north of the Salton Sea. The southwestern flank of the valley is formed by the rugged Santa Rosa Mountains. These are a part of the Peninsular Ranges batholith and appear as a southern continuation of the SJM. The Santa Rosa Mountains appear to have been exhumed during two phases of Neogene extension, based on 29 AHe ages (Fig. 2) (Mason et al., 2017). An initial phase of exhumation resulted from 8–1.2 Ma displacement along the low-angle West Salton detachment fault (Axen et al., 1998; Shirvell et al., 2009) with exhumation rates of ~0.3 mm/yr, interpreted to relate to the widespread extension occurring in the Gulf of California rift (Bennett et al., 2013; Dorsey et al., 2011; Oskin and Stock, 2003; Seiler et al., 2011). This has been followed by exhumation at ~1.3 mm/yr since 1.2 Ma due to high-angle normal faulting along the western flank of the Santa Rosa Mountains and western part of the central Salton block, interpreted to result from transtension between strands of the newly formed San Jacinto fault (Mason et al., 2017). The kinematics of this Quaternary extensional tilting also match the expected broad uplift of the Salton block due to transpression along the SAF. The central Salton block is defined as the basement block between the SAF and San Jacinto fault that underlies Coachella Valley fill and includes the Santa Rosa Mountains, which appears to be tilted to the east based on geophysical and geomorphic evidence (Dorsey and Langenheim, 2015).

Smaller zones of convergence and minor uplift within the Coachella Valley include the Indio and Mecca Hills, both of which have been produced by near-field transpression along the SAF. Moser et al. (2017) measured young apatite and hematite apatite and hematite (U-Th)/He cooling ages cooling ages from crystalline blocks adjacent to the SAF just north of the Salton Sea in the Mecca Hills (Fig. 2). These data established a 10^5–10^6 yr record of focused exhumation and faulting along narrow fault blocks in a 5-km-wide transpressional flower structure adjacent to the SAF.

Based on these constraints for the uplift and exhumation history of blocks bounding the Coachella Valley, we sought to answer several focused questions with minor additional sampling. First, we sought to confirm the results of Wolf et al. (1997), which were obtained with early AHe methodology, to verify that a Neogene exhumation history of the SJM cannot be discerned. Second, we sought to add cooling ages for the LSBM to the southeast of Long Canyon, to test whether the block uplift pattern remains consistent along strike. We also measured several ages in the Mecca Hills prior to

the publication of Moser et al. (2017), which thus offer corroboration of their findings. Finally we conducted topographic analysis and reconstructed the distribution of an old erosion surface, to constrain the uplift pattern of the ranges.

METHODS

Topographic Analysis

We examined topographic metrics as a preliminary assessment of the differences in form of the major tectonic blocks and how these may relate to uplift history and structure. Several topographic metrics were extracted for select basins located in the different zones of the study region. Analysis included catchment-averaged hillslope gradient (which is commonly positively correlated with denudation rate; Binnie et al., 2008; DiBiase et al., 2010), elevation distribution (hypsometric integral, or HI), and stream profiles, including normalized steepness indices (k_{sn}) of slope-area relationships. The HI parameter (0–1) is useful for comparing the distribution of elevation within basins, thus characterizing whether topography is in a state of landscape disequilibrium and more plateau like (i.e., convex, with a higher fraction of area at higher elevations and high HI, e.g., ~0.6), or spikier and in a state of erosional equilibrium (i.e., concave, with a higher fraction of area at lower elevation and low HI, e.g., ~0.4) (Strahler, 1952; Pike and Wilson, 1971). The longitudinal form of bedrock channels is also useful for characterizing or even quantifying uplift and erosion. Longitudinal profiles graphically indicate concavity or convexity (i.e., knickpoints). More powerful is channel k_{sn}, which is derived from the power-law relationships of drainage area (A) and local channel gradient (S) in bedrock channels: $S = k_s A^{-\theta}$, where k_s is steepness index and θ is channel concavity index (Hack, 1957; Flint, 1974). Under certain conditions, k_s and θ can be used to constrain incision and uplift rates along or between channels based on the stream-power incision rule (Howard and Kerby, 1983; Snyder et al., 2000; Whipple and Tucker, 1999; Kirby and Whipple, 2001). Channel profiles in turn can be compared by computing a normalized channel steepness index (k_{sn}) for a reference concavity ($\theta = 0.45$), thereby providing an indication of how incision rates vary due to localized uplift or transient adjustments to base level between or along basins (e.g., Wobus et al., 2006; Crosby and Whipple, 2006; Kirby et al., 2007; Rossi et al., 2017).

We measured these topographic parameters in basins in the LSBM, SJM, and Santa Rosa Mountains using 1/3-arc-second, 10-m-resolution U.S. Geological Survey digital elevation models and Matlab and ArcGIS scripts available online including at Geomorphtools (Whipple et al., 2007; http://geomorphtools.geology.isu.edu). We analyzed 22 basins in total, including seven basins along the eastern escarpment of the LSBM, three that drain the SBM and partially cross the LSBM, four that drain the SJM (including one that overlaps the erosion surface), three transitional basins between the SJM and Santa Rosa Mountains, and five that drain the western flank of the Santa Rosa Mountains (Fig. 3). Average basin statistics discussed below for the basins from these four zones exclude basins that cross multiple domains (e.g., include a portion of the erosion surface). Results are consistent to within ±10% of parameters reported for select basins in Rossi's (2014) study of erosional dynamics, where basin analyses approximately overlap (basins 2 and 3 of the SJM and basin 16 of the LSBM in this study match the sample locations for Rossi's [2014] samples SJ-09-01, SJ-09-03, and LSB-09-02, respectively). We interpreted these results in light of the overall form of each block, including the spatial distribution of slope (Fig. 4). We also examined the character of range fronts (i.e., fan entrenchment, sinuosity, valley width, triangular facets) similarly to the method of Bull (2007) to characterize the relative degree of recent tectonic activity.

Thermochronometry

We measured 11 new apatite AHe ages in the SJM, LSBM, and Mecca Hills (Fig. 2; Table 1). AHe dating is based on radiogenic production of ^{4}He from ^{235}U, ^{238}U, ^{232}Th, and ^{147}Sm in the mineral apatite (Farley and Stockli, 2002; Ehlers and Farley, 2003). Helium diffusion in apatite occurs over the temperature range of 40–85 °C, which is known as the helium PRZ. Closure temperature of the AHe system depends on cooling rate, grain size and morphology, alpha ejection, and radiation damage, but is typically 55–75 °C under normal conditions (Farley and Stockli, 2002; Ehlers and Farley, 2003; Shuster et al., 2006). Samples were collected mainly to augment previously published data sets in the region.

New AHe ages were measured at Virginia Tech (Blacksburg, Virginia, USA) on single- and multi-grain aliquots using standard techniques (Spotila and Berger, 2010; Mason et al., 2017). Multiple replicates of each sample were measured (three to five) to reduce uncertainties. Apatite in dated samples was abundant, large (~60–80 μm radius), and free of obvious microinclusions and flaws. Helium was outgassed in Pt tubes in a resistance furnace (20 min at 950 °C, with re-extract) and measured using quadrupole mass spectrometry with ^{3}He spike, with ^{4}He detection blanks of ~0.2 fmol. Parent isotopes were measured at the University of Arizona (Tucson, Arizona, USA) by isotope dilution (^{233}U, ^{229}Th, and ^{152}Sm spike) and inductively coupled plasma mass spectrometry. All ages reported on Figure 2 and interpreted below are the average ages of all individual alpha ejection–corrected age determinations (i.e., aliquots) for the sample (see Table 1). Estimated analytical age uncertainty is ~5% (1σ) based on precision of each measurement. Reported uncertainties for mean ages are the standard deviation (1σ) of replicates (Table 1). The average observed uncertainty of these samples is 16% (1σ), which is higher than predicted, yet typical for natural samples (Spotila and Berger, 2010; Mason et al., 2017). Six of 39 age determinations were considered to be anomalously old (shown with gray background on Table 1), in that they were >50% older than the sample average. Mean ages reported in Table 1 and Figure 2 exclude these outliers, which are likely due to unidentified ^{4}He contamination. In our experience, this is a typical frequency of outliers (Spotila and Berger, 2010; Mason et al., 2017).

Ages reported here are interpreted qualitatively only, to infer the presence of recent exhumation associated with the modern tectonic regime and

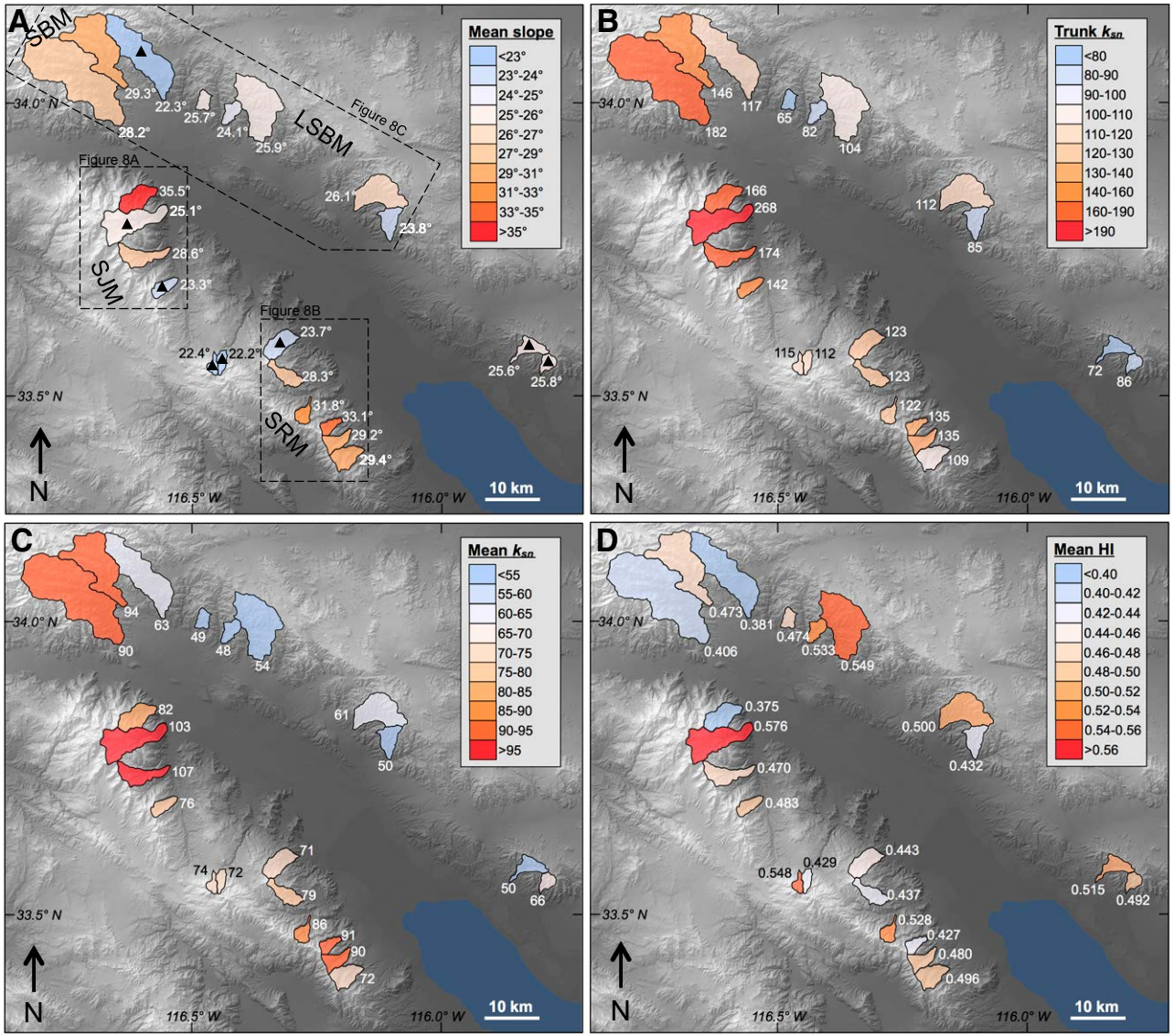

Figure 3. Basin statistics for topographic analysis, Coachella Valley. (A) Mean hillslope gradient of the catchment. (B) Mean value of normalized steepness index (k_{sn}) for the trunk stream. (C) Mean k_{sn} of all streams in the catchment. (D) Mean hypsometric integral (HI). Average basin statistics reported in the text for each area exclude basins noted by triangles in A, which are small or which overlap multiple topographic domains (e.g., erosion surfaces, alluvial valleys, multiple ranges). Location abbreviations are as in Figure 2. Basin numbers are indicated in Figure 8.

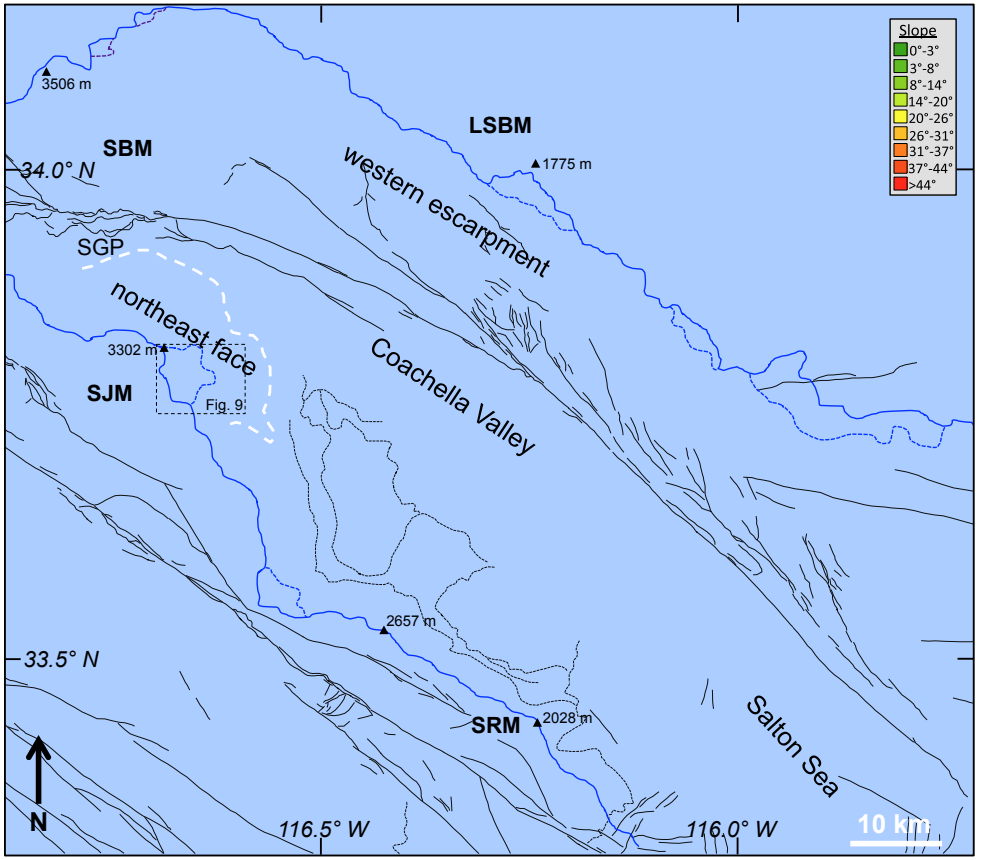

Figure 4. Hillslope gradient map of the Coachella Valley region. Slopes range from low (green) to high (red). Blue line indicates the main catchment divide for the Coachella Valley. Dashed blue lines occurring inward of the main divide represent low-gradient areas at high elevation that fall within the Coachella Valley catchment. These parcels appear to have recently been captured by the Coachella basin, but have yet to adjust to the change in base level. White dashed line in the San Jacinto Mountains indicates the general boundary between granite to the southwest and gneiss and mylonite to the northeast (Rogers, 1965). Faults are labeled in Figure 2. LSBM—Little San Bernardino Mountains; SBM—San Bernardino Mountains; SGP—San Gorgonio Pass; SJM—San Jacinto Mountains; SRM—Santa Rosa Mountains.

to reconstruct the geometry of block uplift using isochrons of older cooling ages. Because we measured these ages primarily for comparison to previous studies and do not interpret details of thermal history of any range block, we did not conduct thermal modeling or take into account the potential effects of parent content and cooling history on radiation damage.

Low-Relief Surface: Background

An important constraint on the magnitude of exhumation in this area is the regional occurrence of a low-relief erosion surface. This surface forms a plateau-like cap atop the crest of the SJM that tapers moderately down to the west (Dibblee, 1981) (Fig. 5). It similarly occurs east of the western escarpment of the LSBM, where it tapers gently down to the east to merge with the low-relief surface of the Mojave Desert (Fig. 6) (Powell, 2002a, 2002b). If this surface marks a horizon of minimal denudation over the time frame of possible block uplift in the current tectonic regime (i.e., during the Neogene; see below), its distribution can be used as an important constraint on the magnitude and geometry of rock uplift.

The characteristics of these erosion surfaces (see below) match those observed throughout the southern Mojave Desert, central Transverse Ranges, and northern Peninsular Ranges (Oberlander, 1972; Minch, 1979; Spotila, 1999; Spotila and Sieh, 2000; Powell, 2002a, 2002b; Seiler et al., 2011). The erosion surfaces of the Mojave Desert and SBM have been interpreted as at least partially relict, rather than having formed primarily under ambient climatic conditions, because they exhibit thick (10–30 m, locally >50 m), in situ granitic saprolite that is in some places argillaceous, heavily oxidized (i.e., dark red), and mineralogically mature (preserving only quartz and altered orthoclase), all of which are characteristics of deep weathering in a humid climate (at least semiarid conditions, but locally mimicking subtropical or tropical weathering) (Oberlander, 1972; Spotila, 1999). Where the saprolite has been stripped away, the surface contains tors and corestones, commonly as a pediment, that also mimic the features of granitic weathering in humid climates (Oberlander, 1974). Although chemical weathering is likely still active locally, such as across the top of the SBM, these observations suggest that the low-relief surface may have developed over a prolonged period prior to uplift of the SBM and marks a horizon of minimal synorogenic denudation (Spotila, 1999).

Support for interpretation of the low-relief surface as at least partially relict and slowly eroding comes from onlapping units. In numerous locations, the saprolitic surface is capped by Mio-Pliocene sediments and basalt flows (generally >6 Ma) (Oberlander, 1972, 1974; Dibblee, 1975; Sadler and Reeder, 1983; Spotila and Sieh, 2000). The depth of incision to the continuous pediment below these caps is generally only 50–150 m, thus also supporting the interpretation that minimal

TABLE 1. APATITE (U-Th)/He (AHe) DATA

Sample	Elevation (m)	Latitude (°N)	Longitude (°W)	Rock type	Mass (mg)	mwar (μm)	He (pmol)	U (ppm)	Th (ppm)	Sm (ppm)	No. of grains	F_T	Corr. age* (Ma)	Average age (Ma)	Standard deviation
15BERC01	253	33.8153	116.1715	Granitic	0.0052	34.5	0.0221	70.1	98.9	49.2	5	0.69	*12.5*		
LSBM					0.0132	85.5	0.0139	21.2	33.7	24.4	1	0.86	7.97		
					0.0047	45.3	0.0037	24.0	30.8	63.8	4	0.73	6.54	**7.77**	1.14 m.y.
					0.0123	76.5	0.0500	65.0	155.4	107.7	1	0.86	8.80		14.7%
					0.0051	48.8	0.0352	41.4	60.7	23.7	2	0.77	*30.3*		
15BERC02	824	33.8293	116.1034	Granitic	0.0196	108.0	0.0296	19.0	9.3	419.1	1	0.87	15.3		
LSBM					0.0030	36.0	0.0022	15.5	7.9	237.0	2	0.65	12.0		
					0.0078	65.6	0.0083	11.7	5.7	343.4	2	0.79	19.0	**15.8**	2.62 m.y.
					0.0107	63.9	0.0183	21.1	8.3	436.7	2	0.79	17.3		16.6%
					0.0106	85.5	0.0123	14.9	6.0	423.6	1	0.85	15.4		
JBCV3	346	33.7590	116.0921	Granodiorite	0.0116	42.8	0.0103	23.0	63.2	82.7	4	0.71	6.22		
LSBM					0.0276	61.3	0.0224	16.4	45.2	65.8	3	0.80	7.08	**6.31**	0.72 m.y.
					0.0085	54.0	0.0063	19.0	54.0	74.7	2	0.78	5.64		11.4%
					0.0028	40.5	0.0040	25.2	40.3	272.7	1	0.72	*10.8*		
JBCV4	1579	33.9273	116.1876	Monzonite	0.0030	32.2	0.0244	26.2	14.2	433.1	3	0.63	81.1		
LSBM					0.0040	50.2	0.0735	22.8	15.6	428.4	2	0.75	*174*	**83.6**	3.62 m.y.
					0.0044	41.2	0.0284	18.1	11.0	382.7	4	0.67	86.2		4.3%
JBCV5	895	33.7340	115.8218	Monzonite	0.0040	38.3	0.0138	5.4	35.3	674.5	4	0.67	66.7		
LSBM					0.0019	29.7	0.0279	16.5	39.3	349.1	2	0.65	*164*	**61.2**	7.75 m.y.
					0.0044	36.5	0.0159	6.6	46.0	855.2	4	0.66	55.7		12.7%
CMHD05	2680	33.8039	116.6455	Monzonite	0.0124	70.5	0.1454	49.8	33.4	86.4	3	0.81	47.3		
SJM					0.0097	40.9	0.1065	48.7	51.3	149.0	5	0.70	49.0	**46.3**	3.32 m.y.
					0.0144	56.6	0.0955	28.2	38.2	108.7	4	0.79	42.6		7.2%
CMPCT03	1014	33.8708	116.6950	Monzonite	0.0129	61.1	0.0489	23.7	28.4	70.4	2	0.82	28.9		
SJM					0.0107	63.0	0.0397	20.9	26.5	66.6	2	0.82	31.4	**30.7**	1.27 m.y.
					0.0203	67.5	0.0833	23.5	29.4	90.2	2	0.83	30.7		4.1%
					0.0120	54.9	0.0403	20.3	21.9	103.3	3	0.79	31.7		
CMPCT04	625	33.8813	116.6841	Monzonite	0.0089	49.2	0.0439	27.0	32.2	62.2	4	0.73	37.1		
SJM					0.0087	92.0	0.0380	24.5	30.7	70.3	1	0.87	29.9	**29.8**	7.35 m.y.
					0.0048	54.9	0.0501	91.2	86.1	493.2	2	0.79	22.4		24.6%
CMPS25	683	33.8416	116.6105	Monzonite	0.0073	45.5	0.0895	89.5	82.6	395.6	5	0.74	28.7		
SJM					0.0080	51.7	0.0947	84.5	93.7	460.8	4	0.76	27.9	**26.1**	3.80 m.y.
					0.0122	49.8	0.0495	41.1	26.4	73.9	4	0.75	21.7		14.6%
CMPC01	168	33.6156	115.9987	Foliated gneiss	0.0039	46.5	0.0012	29.2	6.6	201.9	2	0.71	*2.74*		
Mecca Hills					0.0154	78.9	0.0039	44.1	12.2	498.0	2	0.82	1.23	**1.03**	0.28 m.y.
					0.0241	112.5	0.0013	13.6	1.6	122.8	1	0.89	0.82		27.6%
CMPC16	141	33.6152	116.0017	Pegmatite	0.0192	83.0	0.0117	7.8	0.9	126.2	2	0.85	16.6		
Mecca Hills					0.0205	88.0	0.0025	3.1	1.0	113.8	2	0.88	7.7	**12.3**	4.46 m.y.
					0.0277	65.2	0.0104	6.8	0.7	134.8	3	0.81	12.6		36.2%

Notes: See Figure 2 for sample locations. mwar—mean weighted average radius; F_T—alpha ejection correction factor (after Farley et al., 1996); Corr. age—alpha ejection–corrected age. LSBM—Little San Bernardino Mountains; SJM—San Jacinto Mountains.

*Ages with gray background (in italic) are considered anomalous and not used to compute the average ages (in bold); see text for explanation.

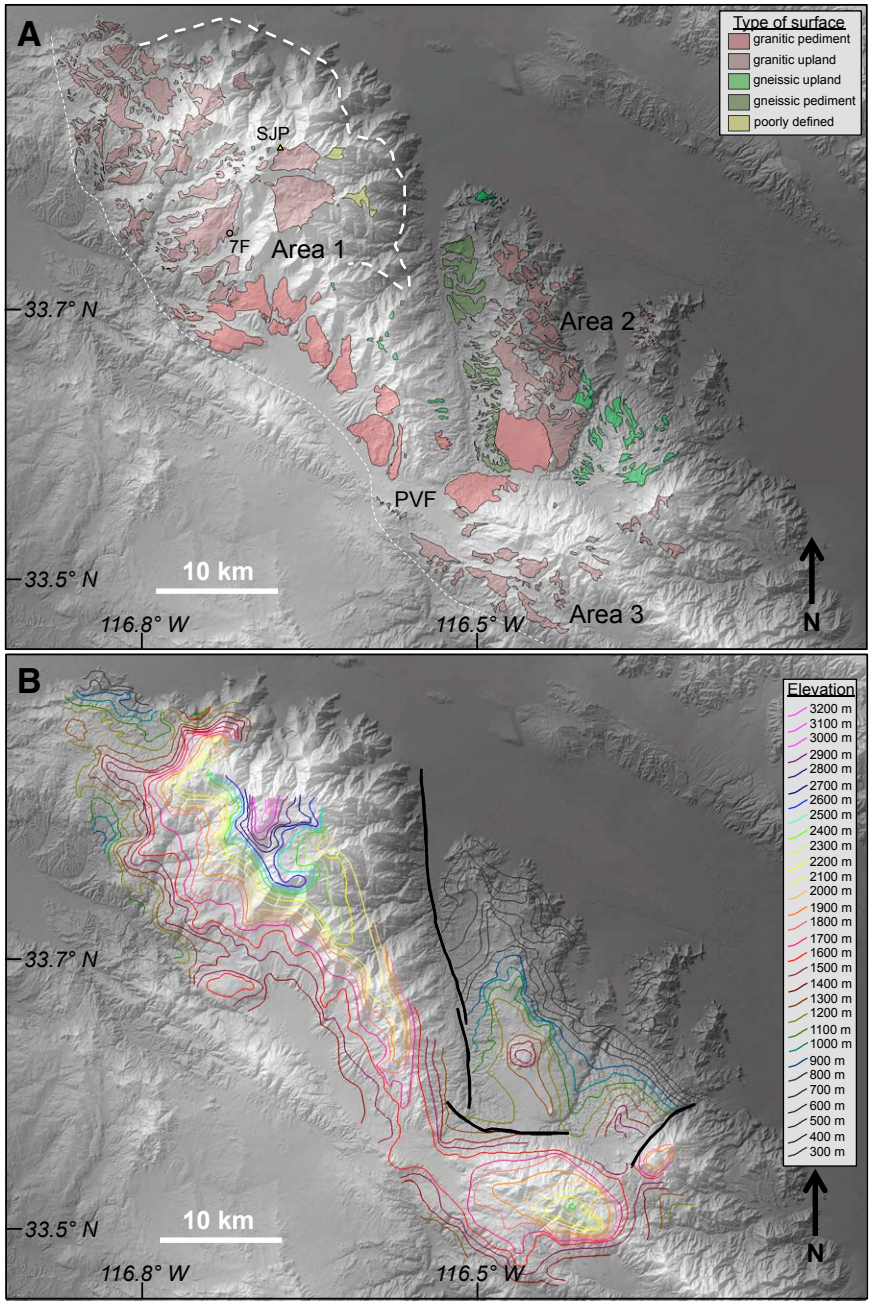

Figure 5. (A) Mapped distribution of the weathered erosion surface atop the San Jacinto Mountains and northern Santa Rosa Mountains. Colors represent different types of surface (bedrock type, pediment versus upland) as indicated by the legend. Thin white dashed line indicates the southwestern limit of mapping. Thick white dashed line indicates the general boundary between granite to the southwest and gneiss and mylonite to the northeast (Rogers, 1965). General location of the Pleistocene Bautista beds is indicated at Pinyon-Vandeventer flats (PVF). SJP—location of San Jacinto Peak. Label 7F is the location of the photo in Figure 7F. (B) Structure contour map of the weathered erosion surface at 100 m contour interval. All types of surface except for "poorly defined" from A were used to constrain contours. Thick black lines indicate faults across which it is difficult to connect contours.

denudation (at slow rates of <30 m/m.y.) has occurred where the surface is preserved (Spotila and Sieh, 2000). Such slow rates of denudation have been verified at 1–10 k.y. time scales from basinwide cosmogenic radionuclide dating in the SBM (Binnie et al., 2008). By comparison, the greater relief between the granitic erosion surface and more chemically resistant lithologies (e.g., metasediment), which occur on average ~400 m higher than the surface in the SBM (Spotila, 1999), suggests a prolonged period of differential, weathering-controlled denudation (i.e., etchplanation, after Twidale [1990]).

The low-relief surface of the Peninsular Ranges of southern California and northern Baja California has been similarly interpreted as relict. This surface is interpreted to be Paleocene to Eocene in age based on the age of distinctive volcanic clasts in gravels that are locally deposited atop it and are in turn overlain by later Tertiary volcanics (Minch, 1979; Axen et al., 2000; Seiler et al., 2010; Rossi et al., 2017). Where preserved, this surface displays similar characteristics of deep weathering that may indicate formation under a more humid climate, of differential lithologies and an absence of surfaces in chemically resistant lithologies (Minch, 1979). Although this surface is not continuous between where covered by Eocene gravels and where exposed in the SJM, its regional presence is suggestive of a broad, low-energy erosional surface that is now in disequilibrium with position relative to current base level.

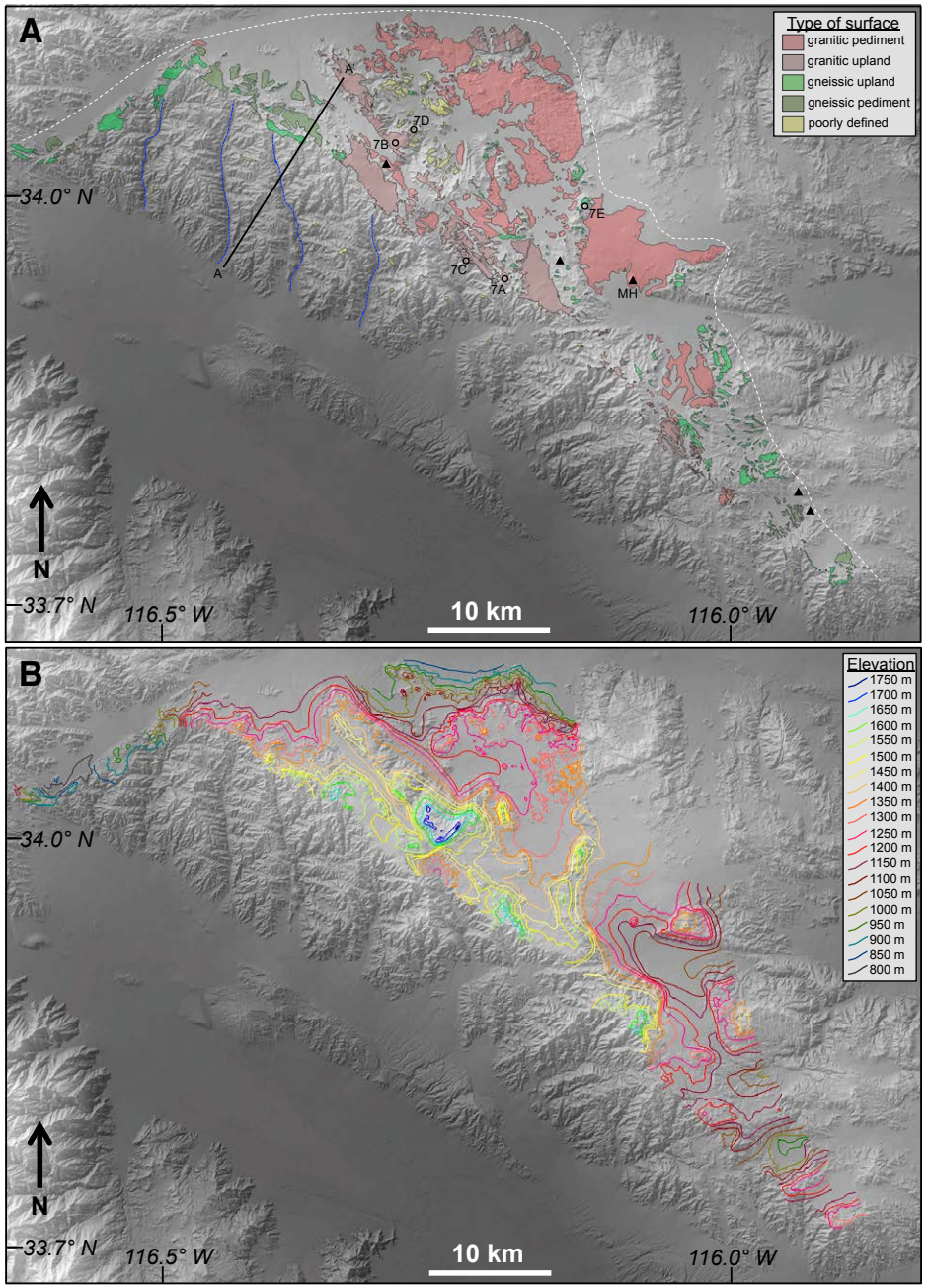

Figure 6. (A) Mapped distribution of the weathered erosion surface atop the Little San Bernardino Mountains. Colors represent different types of surface (bedrock type, pediment versus upland) as indicated by the legend. White dashed line indicates the northern and eastern limits of mapping. Blue dashed lines are trunk streams draining the western escarpment that appear to be rotated counterclockwise relative to the range front. Black triangles indicate locations of Tertiary volcanics atop the erosion surface (MH—Malapais Hill). Labels 7A–7E are locations of photos in Figure 7. Line AA′ refers to the profile in Figure 12. (B) Structure contour map of the weathered erosion surface at 50 m contour interval. All types of surface except for "poorly defined" from A were used to constrain contours.

These interpretations of the regional erosion surface as a marker of minimal Neogene denudation are consistent with the coincidence of the surface with old (i.e., Cretaceous) low-temperature cooling-age isochrons throughout the area. AHe and AFT ages measured from granitic bedrock on this surface are consistently 50–70 Ma and mark a regional horizon of rapid Late Cretaceous cooling associated with the Laramide orogeny that was followed by slow denudation or crustal stasis (Miller and Morton, 1980; Silver and Chappell, 1988; George and Dokka, 1994; Wolf et al., 1997; House et al., 1997; Spotila et al., 1998; Blythe et al., 2000; Cecil et al., 2006; Sabala, 2010). Within the Big Bear plateau of the SBM, for example, AHe isochrons appear to be parallel to the erosion surface, both of which are folded due to deformation on faults in the past few million years (Spotila and Sieh, 2000). The simplest interpretation of how these two independently formed, now-arched surfaces could be coplanar is that they originated more-or-less horizontally and were subsequently co-deformed. This is consistent with the idea that there was a low-relief, subhorizontal weathering surface in the region prior to uplift over the past few million years.

Other work on erosion surfaces, in particular pediments, in the southwestern United States cautions against the strict interpretation of the weathered erosion surface as a time-distinctive, relict horizon. This previous work emphasizes that pediments are dynamic, continually evolving surfaces along which weathered debris is actively transported from exposed bedrock landforms to depositional aprons via a thin veneer of alluvium

and migrating fluvial channels (Nichols et al., 2002, 2005; Strudley et al., 2006; Dohrenwend and Parsons, 2009; Pelletier, 2010). Pediments have been shown to be actively evolving in a variety of climates, including arid desert environments, and as such should not universally be considered relict landforms (Dohrenwend and Parsons, 2009). Pediments may also evolve due to a specific set of evolving processes, related to back-wearing of an uplifted block, isostatic rebound and stripping of the neighboring piedmont, and maintenance of a balance between weathering and continual removal of regolith (Pelletier, 2010). This means that their origin is complex and that they are not necessarily reliable markers of subsequent uplift. Low-gradient erosional benches, as well as local bedrock tors, are also hypothesized to form autogenically above base level due to perturbations in climate and local removal of saprolite, which enables surface lowering above and below due to more rapid weathering beneath the preserved saprolite cover than atop bare bedrock surfaces in the intervening tors (Wahrhaftig, 1965; Strudley et al., 2006; Calvet et al., 2015). These surfaces are in turn dynamically influenced by changes in climate and may be incised or stepped, or exhibit variable alluvial cover.

Nonetheless, previous studies agree that pediments tend to form in areas of slow denudation and in the absence of tectonically driven base-level lowering (Nichols et al., 2002; Dohrenwend and Parsons, 2009; Pelletier, 2010), implying that they can constrain rock uplift where preserved atop mountains. This and other evidence, including the onlapping Mio-Pliocene units and the validation of minimal denudation based on thermochronology and cosmogenic radionuclide dating, present a convincing argument that these erosion surfaces can be considered as pre-orogenic erosion surfaces in the spirit of Calvet et al. (2015).

Low-Relief Surface: Observations and Reconstruction

We mapped the low-relief erosion surface manually based on observations from the LSBM and SJM using high-resolution satellite imagery draped onto digital topography in Google Earth. Based on the first author's prior experience mapping surfaces in the SBM using 1:30,000-scale aerial photographs, Google Earth provides better spatial resolution and ease of visual manipulation. We generally viewed the landscape at a variable scale down to ~1:5000 while mapping, and mapped boundaries to a horizontal resolution of ±25 m on well-defined surfaces, ±50 m where poorly defined, and almost always better than ±0.1 km. We mapped the surface across a 1000 km^2 area of the LSBM and a 1400 km^2 area of the SJM. The area mapped in the SJM included the entire mountainous area to the east of the thin white dashed line in Figure 5A (i.e., all of the way to the alluvial valley). The area mapped in the LSBM included the entire mountainous area west of the thin, white dashed line in Figure 6A, including the rugged escarpment that drops down to the west to the alluviated Coachella Valley. We mapped 591 polygons of the surface in the LSBM and 373 in the SJM. Continuous mapped patches ranged from ~0.002 km^2 to 39 km^2 (a large pediment in the LSBM). Across overlapping areas mapped both in this study and by Spotila (1999), we found that our current mapping had greater detail in the boundaries of defined polygons.

The weathered surface atop the LSBM is extensive and easily identified. It is most reliably identified by the presence of rounded loose corestones and in situ tors (including large irregular suites of tors, or inselbergs) (Fig. 7A). It is best developed on granitic bedrock, although it may also be defined in granitic gneiss (Figs. 5, 6). Where the surface is developed at the top of positive-relief forms (e.g., atop plateaus), it is generally convex and has a low gradient (commonly <3°) with a rounded but distinct slope break to the steeper surrounding hillslopes (Figs. 7B, 7C). These low-gradient uplands thus stand in obvious contrast to the surrounding topography, similar to areas of drainage basin disequilibrium due to base-level fall, where knickpoints mark the boundary between adjusted and relict topography (Crosby and Whipple, 2006). The surface was mapped continuously across where upland flats grade into flanking hillslopes marked by bare, rounded bedrock forms (i.e., tors). Only uplands with a mappable length of continuous, subhorizontal surface were classified as the erosion surface, thereby excluding narrow, rounded, low-slope patches on convex ridges that lack corestones or a sharp slope break to surrounding steeper hillslopes (Fig. 7D). Some of these small, low-slope patches occur along convex ridges extending down the western escarpment (Fig. 6A, shown in yellow), which we have interpreted to most likely be the result of normal hillslope processes rather than as a relict surface. As a result, these patches are not used in construction of contours of the relict surface. In contrast to these sporadic convex ridges, much of the surface on the LSBM plateau to the east can be mapped as semicontinuous, including very large patches of unbroken relict surface. Although some patches of surface were continuous, we emphasize that the mapped surface represents the occurrence of specific geomorphic observations, rather than a unique, contemporaneous structural horizon.

Approximately half of the mapped surface in the LSBM, particularly in the Joshua Tree National Park area, consists of pediments. Pediment surfaces form valley flats adjacent to the bounding hills and are typically expressed as incised, bare bedrock surfaces. Locally the surface on pediments can be traced continuously across steeper, rounded bedrock forms on hillsides to flat upland surfaces. In these cases, the bounding hillslope appears to be a relict positive-relief form (i.e., was exposed during prolonged weathering), rather than a back-wearing slope as typically observed on pediments (Pelletier, 2010). Also unlike many classical pediments, in which the bounding slope does not reflect lithology (Pelletier, 2010), many pediments in the LSBM are clearly lithologically controlled (Fig. 7E). In these cases, the lowland granitic surface abuts ridges and positive-relief forms that are cored by gneissic or other metamorphic lithologies, with typical elevation differences of ~100–300 m.

In a few scattered locations in the LSBM, onlapping volcanic rocks define the surface as relict (Fig. 6). These include several small exposures of ca. 16 Ma hypabyssal basalt (at Malapais Hill; Fig. 6) and other possibly younger basalt flows (Powell, 2002a, 2002b; Muller et al., 2014). The areal extent

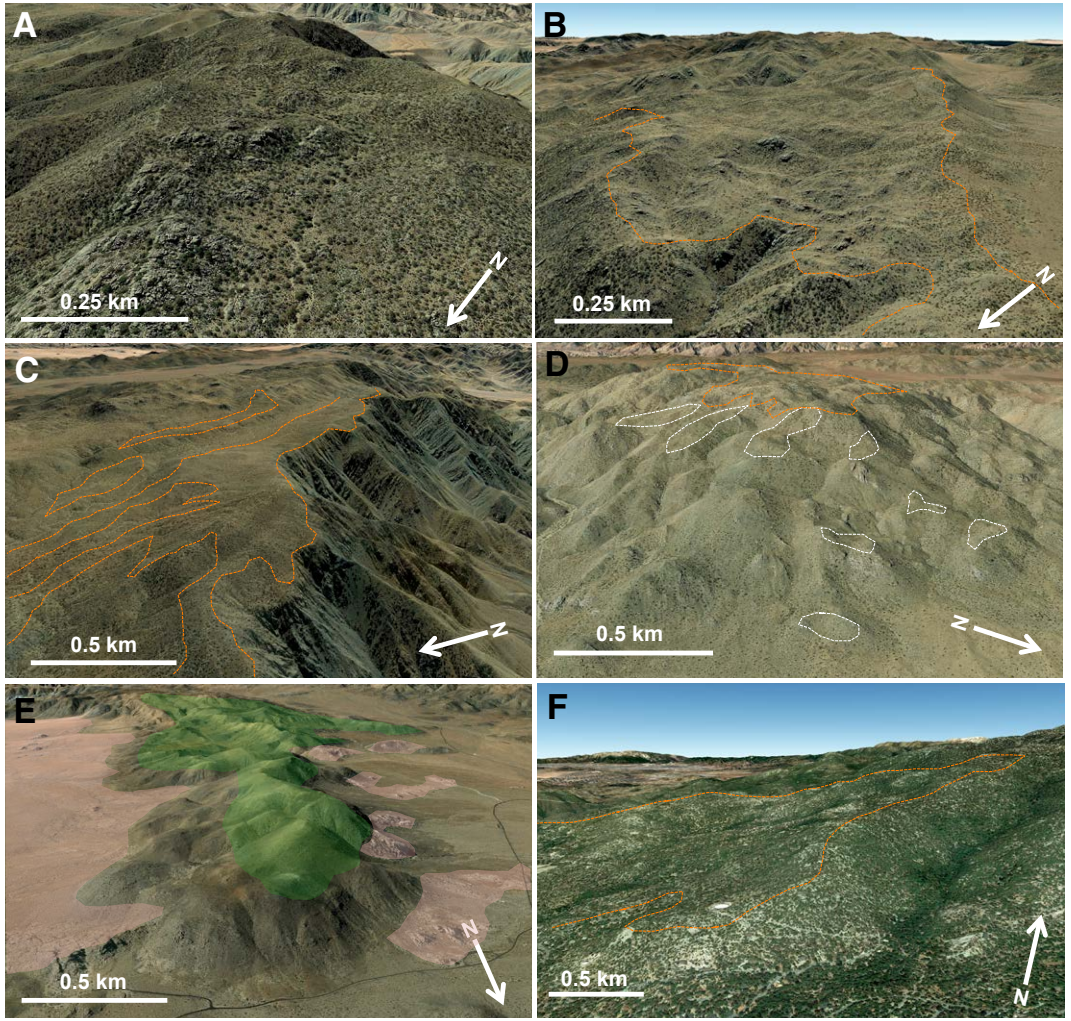

Figure 7. Representative three-dimensional perspective images from Google Earth of the weathered erosion surface in the Little San Bernardino Mountains (LSBM) and San Jacinto Mountains (SJM). Locations are shown in Figures 5 and 6. Orange dashed lines denote the mapped surface. (A) Typical granitic landforms present on much of the erosion surface in the LSBM, including low tors and interlocking corestones. These features are characteristic of the bedrock-saprolite interface under conditions of deep granitic weathering. Image location: 33.941°N, 116.199°W. (B) Representative patch of erosion surface in the LSBM. Note the obvious, rounded slope break from the low-gradient, rolling topography of the erosion surface to the incised region to the north. A similar abrupt slope break occurs to the southwest, which may follow along an old fault separating the patch of surface from the alluviated valley. Note the granitic landforms in the center. Image location: 34.042°N, 116.300°W. (C) Another representative patch of low-relief erosion surface in the LSBM. The sharp slope break on the west corresponds to the asymmetric divide and drop to the western escarpment. To the north and east, the patches of surface are broken by areas of moderate dissection, with more subtle, rounded slope breaks. Image location: 33.953°N, 116.233°W. (D) Gentle, convex ridge surfaces (white dashed lines) in the LSBM that were not classified as proper erosion surface but are marked in yellow on Figure 6. Although granitic landforms typical of deep weathering occur on these surfaces, they were considered too poorly defined (i.e., no clear slope break, too-limited distribution of low gradient) to map. Erosion surface was mapped on the higher topography. Image location: 34.049°N, 116.275°W. (E) Example of etchplanation on the erosion surface of the LSBM, in which lithology controls elevation and surface morphology. The rounded ridge that is shaded green consists of Precambrian gneiss, which sits 250–300 m higher than the surrounding, low-relief granitic pediment (shaded pink). There are many examples in the LSBM like this in which differential weathering and erosion appear related to lithology. Image location: 33.995°N, 116.131°W. (F) Representative patch of erosion surface atop the western flank of the SJM. The slope break, such as with the drainage to the east, is generally more rounded and difficult to define than in the LSBM. The surface is also more hummocky and dissected. Image location: 33.760°N, 116.714°W.

of Mio-Pliocene units is less extensive than in the SBM, however. Based on limited reconnaissance, the erosion surface in the LSBM also does not exhibit the types of exposures described in the SBM by Spotila (1999) of thick saprolite capped by argillaceous soils.

The low-relief surface of the SJM is generally not as well preserved or defined as in the LSBM. Although the largest patches of the surface in the SJM (maximum 26 km^2) are comparable in dimensions to those in the LSBM, most patches tend to be smaller (Fig. 5). There is also greater uncertainty in the boundaries of mapped surface polygons in the SJM. This is in part due to the terrain and heavier vegetation cover of the higher SJM plateau. Individual patches of the surface in the SJM display less-distinct breaks in slope between relict and rejuvenated areas (Fig. 7F). Whereas horizontal uncertainties in mapped surface edges are <0.1 km in the LSBM, they are commonly >0.2 km in the SJM. The SJM surface tends to be more incised than in the LSBM, particularly in the north (Fig. 5A, area 1), where minimum slopes of mapped weathered surface patches are considerably steeper (~8°) than in the LSBM (~3°). Despite greater uncertainty, however, we are still reasonably confident that a deeply weathered surface caps the SJM. This is corroborated by field observation of weathered granite landforms across the area, including the upper plateau surface to the southeast of Mount San Jacinto Peak and the large field of surface patches sloping down to the west. Dorsey and Roering (2006) also reported deep regolith atop the basement beneath the Pleistocene Bautista beds in the southern end of the SJM. The conclusion that a westward-sloping erosion surface occurs in the SJM is also supported by the westward dip of isochrons and other markers in the crystalline bedrock (Ague and Brandon, 1992; Wolf et al., 1997).

The vertical resolution of the reconstruction of the deeply weathered surface is also better in the LSBM than in the SJM. We contoured elevations of the weathered surface, including where developed on both monzonite and granitic gneiss, to a 50 m contour interval in the LSBM and 100 m contour interval in the SJM (where relief is almost double) (Figs. 5B, 6B). The degree to which these contours constrain the magnitude of denudation or surface uplift is unclear, however. In the SBM, Spotila and Sieh (2000) reconstructed rock uplift to ±100 m using the weathered erosion surface, but this was in part because the surface was mapped in the lower footwall blocks surrounding the range, which thus provided an idea of the original, pre-uplift form of the surface that could be differenced with the modern distribution to estimate the residual uplift. In contrast, we do not have constraints on the geometry of low-relief surfaces in the LSBM and SJM prior to recent uplift, and as such do not consider the contours of surface elevation to be reliable indicators of uplift geometry. However, they do likely mark a topographic horizon that has experienced minimal post-uplift denudation, and as such define a horizon that may be informative when compared semiquantitatively to the structures that may have been responsible for uplift.

RESULTS AND INTERPRETATIONS

Topographic Analysis

The distribution of slope in the region demarcates the major tectonic blocks (Fig. 4). Nearly all of the mountain blocks surrounding the Coachella Valley display high slope. The LSBM to the northeast of the valley display a moderately steep western escarpment that transitions abruptly across an asymmetric divide to a more gently sloping plateau surface to the northeast. The SJM to the west of the valley display an even steeper range front, which is among the most rugged landforms in southern California (DiBiase et al., 2018), but this too gives way to a gentle westward-tilting plateau surface above the divide. Both the LSBM and SJM thus have the appearance of tilting away from the Coachella Valley. The southeastern flank of the SBM is steep throughout, but gives way to the Big Bear plateau to the north, which, in combination with other fault blocks, has a domal appearance due to SAF-controlled transpression originating in San Gorgonio Pass (Spotila et al., 1998). In contrast, both flanks of the Santa Rosa Mountains to the west of the Salton Sea display high slope, due to normal faulting and eastward tilting of the central Salton block between the SAF and San Jacinto fault (Dorsey and Langenheim, 2015; Mason et al., 2017).

Average catchment statistics indicate moderate differences between the major crystalline blocks bounding the Coachella Valley. Mean slope is higher in catchments in the SJM (32.1°, n = 2; excluding basins 2 and 4, which partially drain the upper erosion surface), SBM (28.9°, n = 2; excluding basin 13, which partially drains an alluvial valley), and Santa Rosa Mountains (30.4°, n = 5; excluding basin 5, which partially drains the upper erosion surface) than along the LSBM western escarpment (25.1°, n = 5) (Fig. 3A). These values correlate with average trunk stream k_{sn} for the same basins, which are lower in the LSBM (89.6) than other ranges (164.0 in SBM; 170.0 in SJM; 124.8 in Santa Rosa Mountains) (Fig. 3B). Mean catchment k_{sn} shows a similar trend (Fig. 3C). In contrast, average HI is highest in the LSBM, but shows minimal overall variation between the zones (0.42–0.50) (Fig. 3D).

Longitudinal profiles and k_{sn} maps also indicate complexity in the erosion of these basins (Fig. 8). Most streams exhibit knickzones that imply elevation reaches that are adjusted to different erosion rates and history (Rossi et al., 2017). For example, basin 2 (Tahquitz Creek) in the SJM exhibits a prominent knickzone that separates the erosion surface at high elevation from the lower, adjusted part of the basin (Fig. 8A). This knickzone corresponds to locally high k_{sn} and is the reason the trunk stream average k_{sn} is 268, which is the highest observed in this study. The knickzone is also clearly a major boundary in the degree of landscape adjustment from the upper, eastward-sloping erosion surface to the steep eastern face that plummets to the Coachella Valley (Fig. 9). A second knickzone occurs at lower elevation, however, and may separate a reach of higher erosion rate below from a lower erosion rate above, indicating recent base-level fall (e.g., Rossi et al., 2017). Lower knickzones are also visible in basins 3 and 4 in the SJM (Fig. 8A). Stream profiles from the Santa Rosa Mountains are less steep overall than in the SJM, yet still display numerous knickzones, apparent as reaches of elevated k_{sn}, that indicate complex uplift or incisional history (Fig. 8B). The stream profiles of both of these

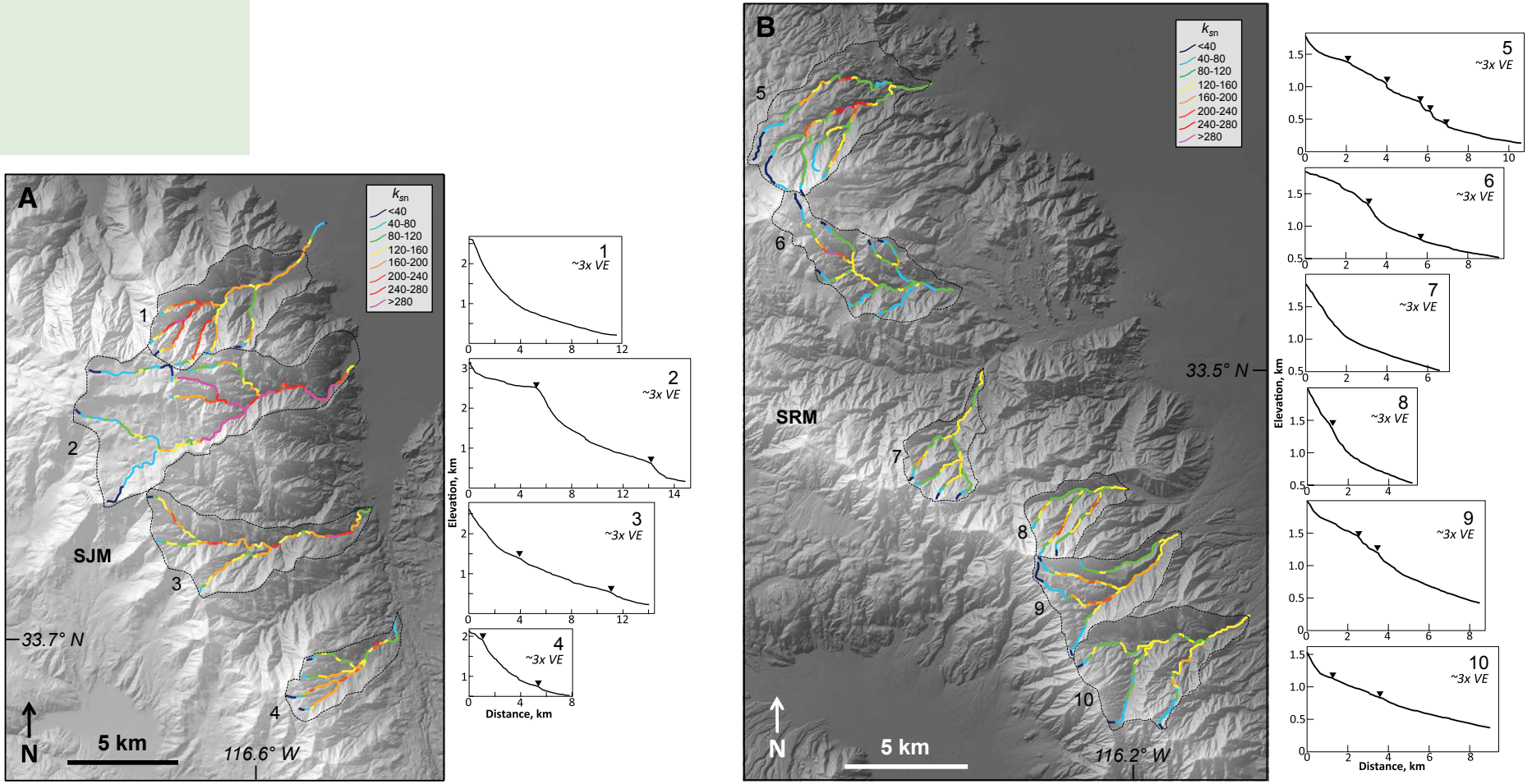

Figure 8. Normalized steepness index (k_{sn}) maps and longitudinal profiles of main streams in studied basins in the San Jacinto Mountains (SJM) (A), Santa Rosa Mountains (SRM) (B), and Little San Bernardino Mountains (LSBM) (C). Values of k_{sn} range from <40 to >280 as shown in the legend. Black triangles denote prominent knickzones on longitudinal profiles. Longitudinal profiles within each region are shown at the same scale. Profiles for the SJM and SRM are plotted with ~3× vertical exaggeration (VE), whereas those for the LSBM are shown with ~8× VE due to the lower relief. Locations of the maps are shown on Figure 3A. SBM—San Bernardino Mountains. (*Continued on following page.*)

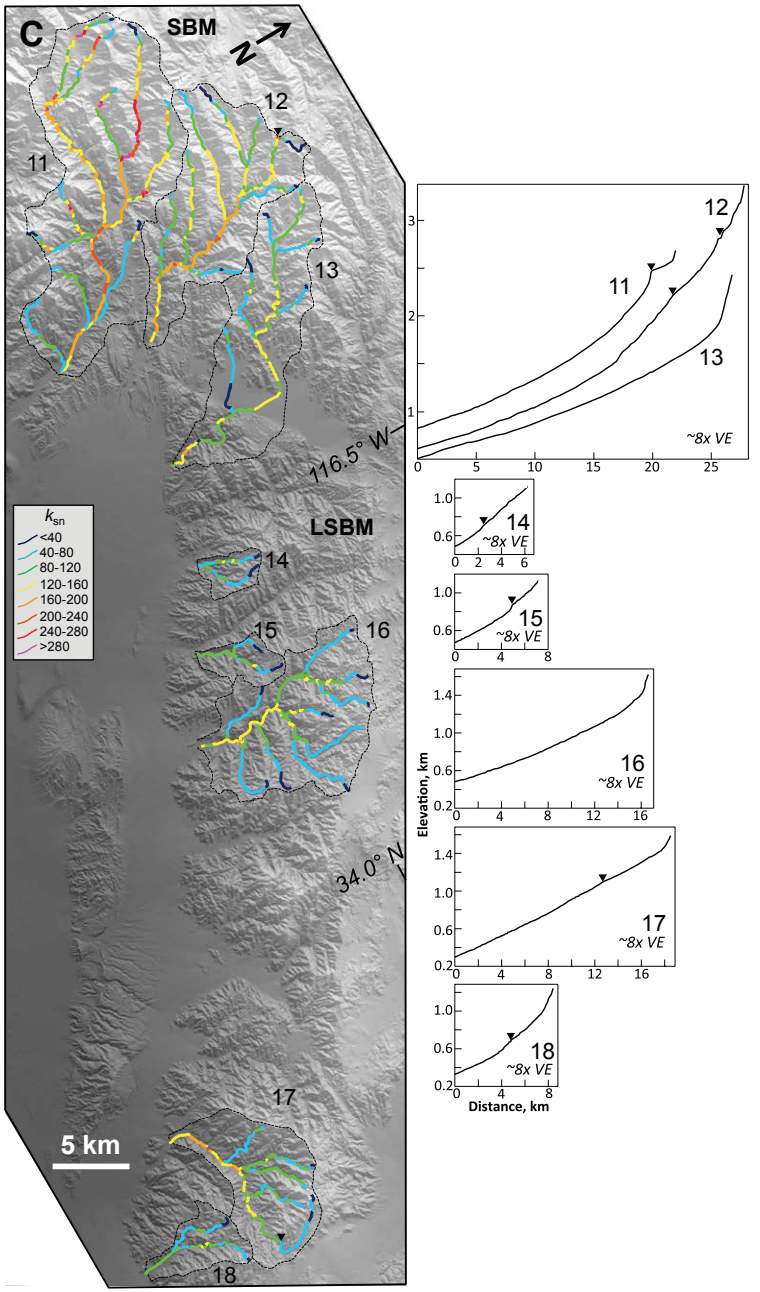

Figure 8 (*continued*).

ranges are therefore consistent with mountain blocks that are experiencing not only active uplift, but uplift rates that have accelerated sometime in the recent tectonic history. In contrast, stream profiles from the LSBM exhibit less-steep profiles with fewer knickzones (basins 13–18, Fig. 8C).

An additional curiosity about streams along the western escarpment of the northern LSBM is map-view orientation. Prominent stream valleys are not oriented normal to the northwest-trending escarpment (i.e., SAF parallel), but instead are systematically oriented north-south, or 30°–40° oblique to the direction of the long-wavelength slope (Figs. 6A, 10). This obliquity is opposite from the sense expected given the 41°–44° clockwise vertical-axis rotation of the eastern Transverse Ranges since the late Miocene (Carter et al., 1987; Langenheim and Powell, 2009). Reversing this tectonic rotation would actually make the prominent stream valleys on the escarpment subparallel to the range front. The obliquity of stream valleys likewise is the opposite sense from what would be expected for progressive clockwise river deflection due to accumulation of off-fault dextral shear along the SAF, although this deflection would be focused more closely (<1 km) on the fault (Gray et al., 2018). The trend of these stream valleys may instead result from differential erosion along bedrock faults. Hislop (2019) mapped north-south–trending faults along these canyons (e.g., Long Canyon fault, Wide Canyon fault, Eureka Peak fault) and interpreted these to be a fault set related to nascent transfer of dextral slip from the SAF to the Eastern California shear zone.

Range-front characteristics of the LSBM and SJM also provide clues to the tectonic uplift history. The fronts of both ranges entering the Coachella Valley are highly sinuous and embayed (Fig. 10), a characteristic that would generally suggest a tectonically inactive range front (Bull, 2007). Mountains that have transitioned into a state of down-wearing may become inundated with alluvium, which buries evidence of faulting and leads to an embayed front. Based on the criteria suggested by Bull (2007), including an embayed front, fan entrenchment, and rounded valley bottoms, the LSBM range front would be classified as "class 3",

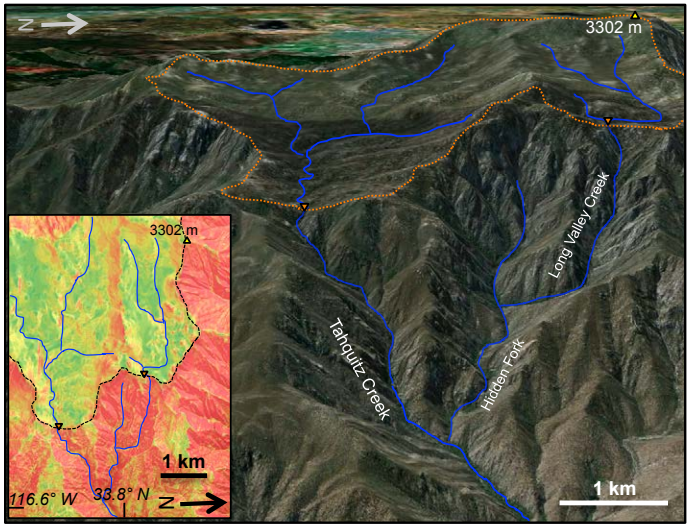

Figure 9. Landscape disequilibrium in the San Jacinto Mountains (SJM), as illustrated in a three-dimensional perspective view from Google Earth. Location is shown in Figure 4. Prominent knickzones (orange triangles) and transitions between the upper erosion surface and lower adjusted landscape that makes up the eastern face of the range are clear in Tahquitz Creek and Long Valley Creek. Stream profile for Tahquitz Creek is shown in Figure 8A (basin 2). Mapped distribution of the weathered erosion surface is denoted by the orange dashed line. Blue lines indicate streams. Inset denotes the slope map of this location, where the gentle slopes (green and yellow) of the upper surface are in stark contrast to the steeper slopes (red) all around. The summit of SJM (San Jacinto Peak) is illustrated by the yellow triangle (3302 m).

or having evidence for slow tectonic activity. Fans along the SJM are less entrenched, while canyons of the SJM are steeper and V-shaped (e.g., gorge at the base of Tahquitz Creek), suggesting a greater degree of tectonic activity that is consistent with the observation of knickzones and elevated k_{sn} discussed above. It is unclear whether the SJM front would classify as "class 2" (rapid tectonic activity), however, given the extreme degree of embayment (Bull, 2007). These qualitative estimates are somewhat consistent with limited cosmogenic radionuclide–based basinwide erosion rates for streams draining these range fronts in the LSBM and SJM (Rossi, 2014; Fosdick and Blisniuk, 2018), which range from 0.04 to 0.24 mm/yr (SJM) and 0.05 to 0.48 mm/yr (LSBM) and are comparable to those of other actively uplifting blocks in the region (e.g., Binnie et al., 2008). It is surprising that the less-steep LSBM basins have, in some cases, higher erosion rates, but more data are required from these range fronts to robustly characterize erosion history (Rossi, 2014).

The degree of embayment of the LSBM and SJM range fronts may be misleading in terms of tectonic activity, due to the high deposition rates in the Coachella Valley supplied by erosion of the surrounding mountain blocks (Fig. 2). We compared these range fronts to other active fronts in the region, which we artificially "flooded" by applying elevation masks (Fig. 10). These elevation masks mimic instantaneous burial by sediment, although they do not take into account the slight decrease in elevation away from the range front due to depositional slope or effects of time on sediment deposition. We manipulated mask heights iteratively to maximize the degree of embayment, to see what depth of sediment might be necessary to convert an active range front into a highly embayed one. Range fronts examined included three normal-faulted fronts (Sierra de San Pedro Mártir, Baja California; White Mountains, California; Toiyabe Range, Nevada, USA), a strike-slip front (SBM and San Andreas fault), and a thrust front (San Gabriel Mountains and Sierra Madre fault, California) (Fig. 10). Sinuosity is evident visually as well as in the ratio of true range-front length to linear range-front length (S, or S_F for flooded range front) (Fig. 10). The sinuous unflooded range fronts of the SJM (S = 2.95) and LSBM (S = 3.84) are closer in sinuosity to the flooded active range fronts (average S_F = 3.03, n = 5) than the unflooded active range fronts (average S = 1.51, n = 5). These results show that burial by only 250–600 m could transform an active front to a highly sinuous one. Because this amount of burial represents only 10%–20% of what has been deposited since the late Miocene in the northern Coachella Valley (Langenheim et al., 2005; Dorsey et al., 2011; Ajala et al., 2019), tectonically active range fronts of the SJM and LSBM may have been overwhelmed by deposition only in the last million years or so. The inundated front that best mimics that of the SJM is that of the Sierra de San Pedro Mártir, which is an active normal-faulted range front with complex uplift history in the same lithology (Peninsular Ranges batholith) along the extending Gulf of California (Rossi et al., 2017) (Fig. 10). Both ranges exhibit irregular, narrow noses that extend like tentacles from the main block of high topography. Whereas the unflooded Sierra de San Pedro Mártir is linear and exhibits clear triangular facets that are connected to higher topography by narrow, isolated ridges, burial hides these facets and leaves the connecting ridges exposed as tentacles, thereby generating extreme range-front sinuosity. The SJM and LSMB may thus have similar normal-faulted origins, but with insufficient duration of time since tectonic activity ceased to have diminished the ruggedness of their respective escarpments.

Low-Temperature Cooling Ages

New AHe ages from the Coachella Valley and surrounding area provide support for the conclusions of previous low-temperature thermochronometry studies and further constrain interpretations of uplift kinematics. Ages from the southern LSBM are consistent with the previous data obtained by Sabala (2010) from the northern LSBM. Five new ages range from 6.3 to 84 Ma and define a rough age-elevation gradient (Table 1; Figs. 2, 11). The age-elevation relationship of a PRZ with an acceleration in exhumation at ca. 5 Ma is supportive of what Sabala (2010) obtained ~40 km to the north at Long Canyon, although the PRZ is shifted ~200 m lower in elevation (Fig. 11). The new data indicate that the block uplift pattern identified at Long Canyon is consistent along strike. Our old ages from

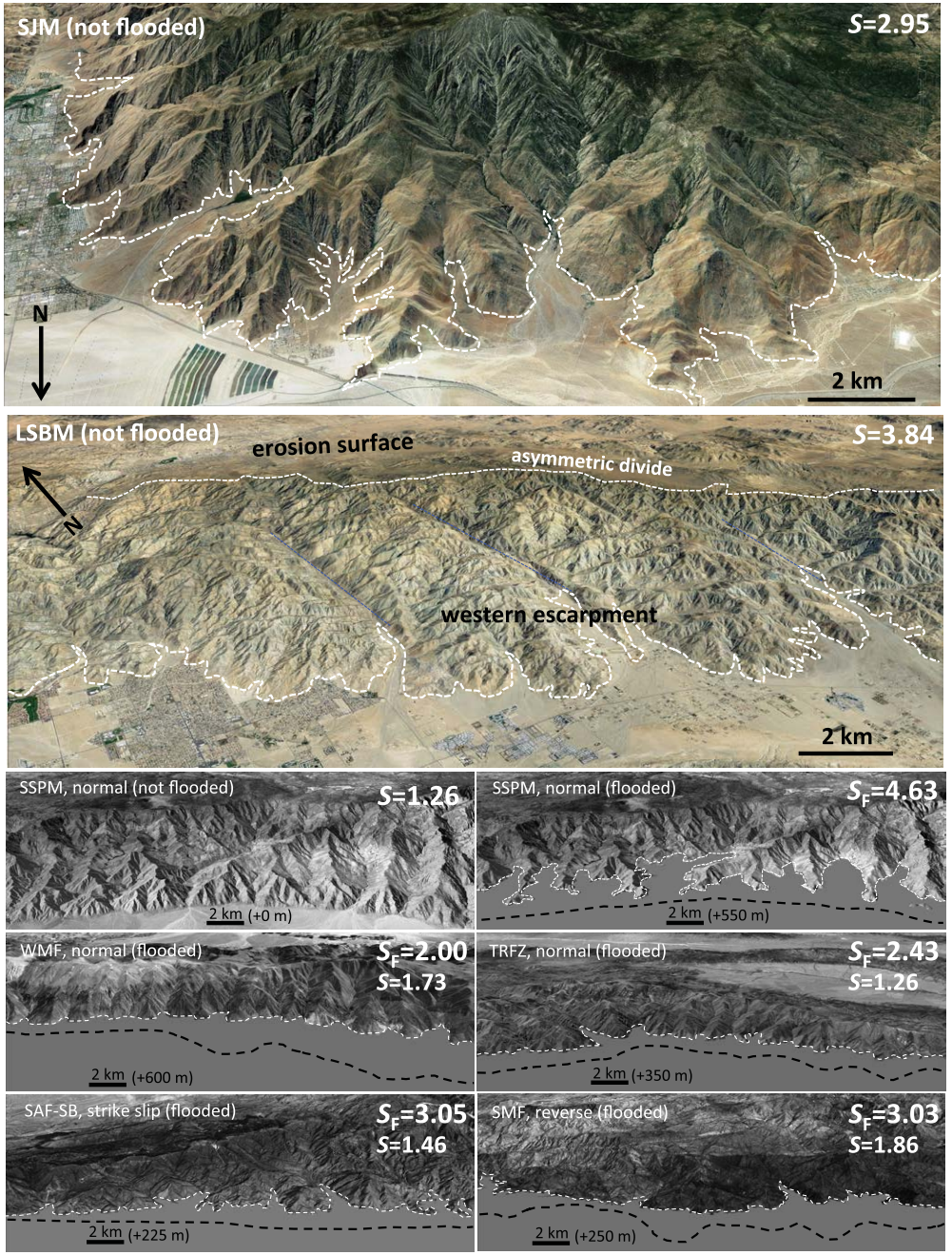

Figure 10. Comparison of the range fronts of the San Jacinto Mountains (SJM) and Little San Bernardino Mountains (LSBM) with other actively uplifting range fronts. In the upper two panels, three-dimensional Google Earth perspective views of the northern face of the SJM and western escarpment of the LSBM are shown. White dashed line illustrates the embayed nature of the hillslope-alluvial interface. In the six panels below, other range fronts with different uplift mechanisms are shown: SSPM—Sierra de San Pedro Mártir (normal faulted, Baja California, Mexico, 30.8702°N, 115.2427°W); WMF—White Mountains fault (normal faulted, California, 37.6860°N, 118.3557°W); TRFZ – Toiyabe Range fault zone (normal faulted, Nevada, USA, 38.9092°N, 117.2488°W); SAF-SB—San Andreas fault (strike-slip faulted, San Bernardino, California, 34.1595°N, 117.2428°W); SMF—Sierra Madre fault (reverse faulted, Pasadena, California, 34.1832°N, 118.0652°W). Each of these panels is 25 km wide. In each panel (with the exception of SSPM, not flooded), the range front is "flooded" by an elevation mask of a given height above the alluvial valley below (e.g., +550 m), as indicated at the base of each panel. Black dashed line indicates the original (unflooded) position of the range front. Height of flooding was adjusted manually to obtain the visually most embayed range front. Note that flooding results in a more sinuous range front in all cases, but the most embayed case that most closely resembles the SJM and LSBM is the Sierra de San Perdo Mártir (SSPM). Sinuosity (*S*, measured as actual length divided by linear length) value of each front is shown in the upper right corner, where a flooded range-front sinuosity is given as S_F. For the five active range fronts, both S_F (for pictured landscape) and *S* (smaller font; given for unflooded case that is not shown in the figure) are provided. Rapid recent deposition in the Coachella Valley may have buried a sharp linear range front with triangular facets and faults responsible for uplift in the SJM and LSBM.

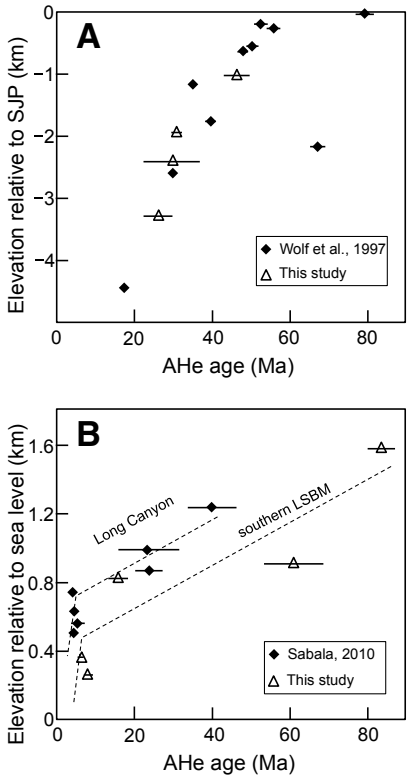

Figure 11. (A) Age-elevation plot for apatite (U-Th)/He (AHe) ages in the San Jacinto Mountains. Ages in this study are compared to those of Wolf et al. (1997). Ages are plotted as elevation below San Jacinto Peak (SJP; 3302 m) based on a 7° tilt down to the west along a north-south axis, as in Wolf et al. (1997). Error bars (1σ) shown for our ages are the standard deviation of replicate measurements (Table 1). Error bars (1σ) shown for Wolf et al. (1997) ages are based on 3% cumulative instrument precision (replicate ages were not measured). (B) Age-elevation plot for AHe ages in the Little San Bernardino Mountains (LSBM). Ages in this study from the southern LSBM are compared to ages from Long Canyon from Sabala (2010). Dashed lines indicate the interpreted age-elevation relationship through a partial retention zone (best-fit regression through older ages) and an accelerated exhumation path beginning at ca. 5 Ma for the two regions, with the southern LSBM showing similar path but ~200 m shift below the Long Canyon path. The interpreted relationship for the southern profile is drawn specifically to illustrate the plausibility that this profile has the same cooling history as the northern profile from Sabala (2010). Error bars shown are 1σ.

the upper LSBM surface are consistent with Late Cretaceous cooling ages measured elsewhere from a regional erosion surface developed in the Sierra Nevada and Peninsular Ranges batholith in the SBM, LSBM, and SJM (Wolf et al., 1997; Spotila et al., 1998; Sabala, 2010), and thus support the hypothesis that the upper surface of the LSBM is a structural horizon of minimal Cenozoic denudation. Our younger ages are comparable to those of Sabala (2010), thus supporting his interpretation that exhumation along the southwestern margin of the LSBM occurred after the SAF became active in the Coachella Valley (i.e., after 5–7 Ma, or after the San Gabriel fault became inactive and the plate boundary changed from transtensional to transpressional; Matti and Morton, 1993). Because we have added only a few new cooling ages that corroborate the results of Sabala (2010), we do not present new modeling or interpretations of the Cenozoic cooling history.

New average AHe ages from the SJM span 26–46 Ma and overlap closely with ages from similar elevations measured by Wolf et al. (1997) (Table 1; Figs. 2, 11). We measured these new ages because the PRZ identified by Wolf et al. (1997) did not include an inflection to younger ages at lower elevation that could be related to the timing of most-recent rock uplift (see Spotila, 2005). The PRZ identified by Wolf et al. (1997) spans 79–17 Ma from peak to base, over an elevation range of nearly 3 km and spanning a structural relief of ~4.5 km (i.e., isochrons are tilted ~7° to the west). Because Wolf et al. (1997) measured ages on 10 mg aliquots of apatite, rather than on carefully screened aliquots of a few (or single) apatite grains (typical mass ~0.01 mg), we speculated that unidentified inclusions or other contaminants could have resulted in overestimation of cooling age. Our new results show that this is not the case, however, as the data fit closely with results from Wolf et al. (1997), despite the difference in analytical techniques. We thus confirm that the base of the SJM crustal section does not necessarily reach the base of the PRZ and thus may not record the timing of uplift of the section from PRZ paleodepth.

The reason the 4.5-km-thick relief section of the SJM fails to expose young cooling ages, whereas ages from the base of the 1.5-km-thick crustal section of the LSBM reveal Neogene exhumation, may be a difference in geothermal gradient. Although these locations are 15 km apart today, restoring dextral slip on the southern SAF since the Miocene (Dillon and Ehlig, 1993; Matti and Morton, 1993; Powell, 1993; Darin and Dorsey, 2013) demonstrates that they were at least 200 km apart when the PRZs were forming. Estimates of Cenozoic geothermal gradient based on thermobarometry and thermal modeling in the eastern Peninsular Ranges in Baja California, 300 km farther south, are 15–25 °C/km (Barton and Hanson, 1989; Rothstein and Manning, 2003; Seiler et al., 2011). In contrast, estimates of geothermal gradient during the Cenozoic used for modeling thermochronometry in the LSBM, SBM, and similar Sierran-type batholithic crust in the Sierra Nevada mountains farther north are typically 20–30 °C/km (House et al., 1997; Spotila et al., 1998, 2001; Cecil et al., 2006; Sabala, 2010). Brady et al. (2006) similarly estimated a high geothermal gradient in the upper crust for the Sierra Nevada batholith based on radiogenic heat production. Whole-rock concentrations of radiogenic elements are generally higher in the Sierra Nevada batholith (3–10 ppm U, 15–25 ppm Th, 3% K, each increasing upward in the crust; Wollenberg and Smith, 1968; Sawka and Chappell, 1988; Brady et al., 2006) than in the Peninsular Ranges batholith (2 ppm U, 10 ppm Th, 2% K; Silver and Chappell, 1988), consistent with a higher geothermal gradient in the Sierra-type crust. It is unclear whether the geothermal gradient in the SJM was low enough to mask late Cenozoic exhumation, however, given that Wolf et al. (1997) determined that ~5–10 °C/km was required to spread the PRZ over such large structural relief.

In addition to data for the LSBM and SJM, two new ages from the Mecca Hills are the youngest measured in this study and match earlier data (Fig. 2). Moser et al. (2017) identified young AHe ages (ca. 1.2 Ma) from a 1.5-km-wide basement sliver between the Painted Canyon and Platform faults, as well as older ages (average of several samples ca. 4–10 Ma) from an adjacent fault block. Our data, which were collected independently of this parallel study, produced similar ages inside

(1.2 Ma) and outside (12.3 Ma) of the Painted Canyon–Platform fault block (Fig. 2). Our reconnaissance work thus matches their more robust data and supports the interpretation that the Mecca Hills have experienced recent, rapid, punctuated rock uplift and exhumation, including inversion of a Plio-Pleistocene valley fill, due to transpression along the southernmost SAF.

Isochron Tilting

Even where low-temperature cooling ages predate the genesis of modern topography, they may still be of use in constraining the kinematics of basement uplift as structural markers. Isochrons of old cooling ages or PRZs can provide marker horizons in crystalline rock that can be used much like stratigraphy to reconstruct the geometry of block tilting and deformation (Spotila, 2005). In the SJM, our new ages match ages from Wolf et al. (1997), and therefore support their interpretation of a 7° ± 2° westward block tilt.

In the LSBM, our data support the results of Sabala (2010). However, we offer a slightly different interpretation of the geometry of block tilting based on the PRZ. Sabala (2010) modeled the cooling history of each sample individually, and thus did not uniquely test whether the vertical suite of samples could be explained with a single cooling history or whether a structure had to be present between samples. Sabala (2010) inferred that an unmapped fault occurs 12 km from the SAF that juxtaposes the younger and older ages, but did not document other evidence for this young fault or constrain what magnitude or sense of displacement would be required by the difference in cooling ages. Although we agree that a fault may be present, we also consider it possible that this change in cooling history results more simply from the inflection in the PRZ–partial annealing zone, or the vertical transition between younger ages that record cooling associated with exhumation over the past 7 m.y. and older ages that do not record the Neogene cooling history. Such age inflections can occur over a very narrow range in elevation and thus be mistaken as structural boundaries between samples of apparently unique cooling history (Spotila, 2005). To what degree a local structure is required to explain this step in cooling ages is not clear. It also seems that such a structure need not have experienced vertical motion, as inferred by Sabala (2010), but rather could simply be a northwest-trending, SAF-parallel dextral strike-slip fault. Any deviation in trend between spatial gradients in cooling history and the fault would therefore result in juxtaposition of cooling histories that could appear to be even more abrupt than an inflection in the PRZ–partial annealing zone. Due to these uncertainties, we completed a simple structural interpretation of the PRZ geometry across the Sabala (2010) transect as an unbroken suite, to quantify what magnitude of northward tilting is required by the data.

An isochron model of Sabala's (2010) AHe ages is presented in Figure 12. The magnitude of isochron tilting in this model is based on adopting the AHe age–elevation gradient observed elsewhere in the region. Because the Sabala (2010) transect spans a long horizontal distance, isochron tilting may obscure true age-elevation relationships. A similar range in AHe occurs as a PRZ over a shorter horizontal distance in the SBM, which is located ~70 km to the northwest and has the same crustal affinity (Spotila et al., 1998). Using the 50 m.y./km age-elevation gradient from the Big Bear plateau in the SBM, we calculated what elevation difference should occur between each AHe sample location in Long Canyon. Where the calculated elevation differed from the actual sample elevation, we tilted the isochrons accordingly. Based on this, isochrons in the Long Canyon PRZ between ages 23.8 Ma and 39.9 Ma can be roughly horizontal (Fig. 12). Isochrons can also be horizontal to the lip of the plateau to the northeast, assuming that the AHe age at the top is ca. 60 Ma (as observed to the southeast in this study and to the northwest by Spotila et al. [1998]). Farther northeast, the isochrons are shown as tilting to the northeast at ~4° to match the slope of the weathered erosion surface (Fig. 12). To the southwest, however, we find that isochrons must tilt upward

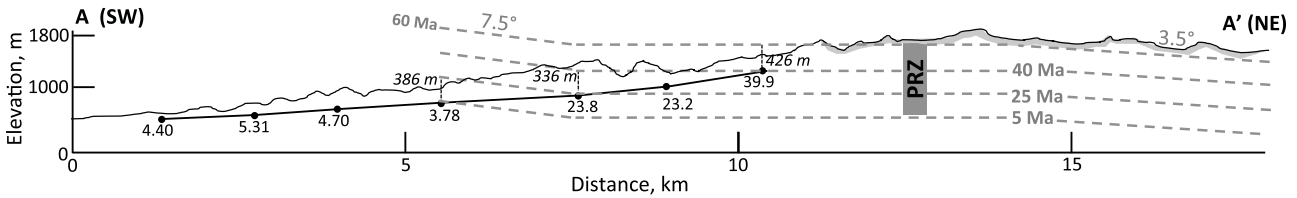

Figure 12. Isochron model of Sabala (2010) apatite (U-Th)/He (AHe) ages along line AA′ (N34°W) drawn normal to the Little San Bernardino Mountains range front and shown in Figure 6A. AHe ages (in Ma) for sample locations along the north-trending Long Canyon are shown at base (black dots, projected onto the line), along with the elevation profile of the profile (solid black line) and the elevation change of the sample transect (thicker black line). Proposed isochrons are shown as gray dashed lines (5, 25, 40, and 60 Ma isochrons). This model assumes a northeast tilt of 3.5° based on the orientation of the weathered erosion surface to the northeast of the western escarpment (gray band shown below topographic profile). The model also assumes a 50 m.y./km age-elevation gradient based on similar cooling observed in the partial retention zone (PRZ) for the Big Bear plateau to the northwest (Spotila et al., 1998). Finally, the base of the PRZ is assumed to be 4.5 Ma, the average age of the four southwesternmost AHe samples on the profile. To fit isochrons with the 50 m.y./km gradient into the short elevation space between the 3.78 and 23.8 Ma samples, isochrons must tilt upward 7.5° to the west. In contrast, the PRZ appears horizontal between the 23.8 Ma age and the weathered erosion surface. This model illustrates that the AHe ages at Long Canyon can be explained by tilting of a PRZ and increase in cooling at 5 Ma, without requiring faults between the 3.78 and 23.8 Ma ages. This does not rule out the Sabala (2010) interpretation, however.

to allow enough elevation span between samples to fit the basal section of the PRZ. Isochrons must tilt upward by ~8° to allow ages to range from 23.8 Ma to 4.5 Ma (the average of the lower-elevation AHe ages in Long Canyon and assumed timing of onset of rapid uplift) between the samples bearing the 23.8 and 3.78 Ma ages (Fig. 12). The result implies that the LSBM are tilted gently downward to the northeast away from the escarpment, mimicking a tilted plateau along a normal fault block.

Although isochrons are not drawn to the southwest of the 3.78 Ma sample (Fig. 12), they may tilt slightly downward to the southwest (parallel to topography), may be horizontal, or may continue tilting upward to the southwest, because the ages farther southwest are equally young (4–5 Ma). The latter may be the most likely scenario based on the cooling-history modeling of Sabala (2010), however. That modeling showed increasing magnitudes of Neogene cooling with increasing proximity to the SAF. For example, a sample within 3 km of the fault may have experienced 3–4 km of exhumation since 7 Ma (Sabala, 2010). This magnitude of exhumation near the SAF is greater than the ~2 km of exhumation that would be required by projecting the 8° up-to-the-southwest isochron to a position over the 4.40 Ma sample (Fig. 12). As a result, local, possibly transpressional, rock uplift near the trace of the SAF is likely required. Because AHe and AFT cooling ages do not become older with distance to the southwest of where our isochrons terminate, however, the isochrons may not dip steeply downwards to the southwest, and thus a structural dome centered along the escarpment (i.e., in the vicinity of the 3.78 Ma sample; Fig. 12) is not likely.

This isochron model implies that observed AHe ages can be explained as resulting from a tilted PRZ, and do not require local uplift or a fault juxtaposing older and younger ages between the 3.78 and 23.8 Ma samples. It is difficult to assign uncertainties to this isochron model, however. It is unclear whether the assumed age-elevation gradient from the SBM truly applies, or what the effective error bars in this gradient are. To assess the sensitivity to this assumed gradient, we also created end-member isochron models using 30 m.y./km and 70 m.y./km age-elevation gradients. In the former case, a simpler isochron pattern results, in which isochrons parallel the weathered erosion surface with an ~4° tilt (down to the northeast) to the location of the 23.8 Ma sample, then steepen to 14° (down to the northeast) farther southwest along the escarpment. In the latter case, isochrons tilt more gently downward to the northeast (~4°) along the escarpment (i.e., between the 23.8 and 3.78 Ma samples), but define a very gentle arch with a down-to-the-southwest panel (1°–3° tilt) between the 23.8 Ma sample and the lip of the escarpment. Although the specific tilt magnitudes differ, both alternative models produce realistic isochron patterns and explain observed ages without requiring a fault or local uplift between the 23.8 and 3.78 Ma samples. We interpret this as reasonable (yet nonunique) evidence for the plausibility that the AHe age pattern represents a tilted PRZ across the LSBM.

Rock Uplift Based on Surface Reconstruction

Reconstruction of the weathered erosion surface provides important new constraints on the geometry of rock uplift in the LSBM. We mapped approximately half of the upper plateau surface of the LSBM as a weathered surface (Fig. 6A). Large alluvial fans form gaps in this surface and obscure mapping of underlying basement surfaces. The weathered surface also wraps around the northwestern tip of the range and drapes downward into Morongo Valley, where it merges with the surface of the SBM. In contrast, the surface is absent along the escarpment southwest of the main divide. The lack of surface remnants along the escarpment confirms that this area has experienced much greater denudation than the upper plateau surface. We hand-contoured all mapped patches of the surface to a 50 m contour interval, regardless of whether the patches were formed on monzonite or gneiss or as pediments (Fig. 6B). As a result, some variation in contour elevation may result from etchplanation or inherited pre-uplift topography. The contours of the weathered surface in the LSBM ranged from 800 to 1750 m (950 m relief), but across the main part of the plateau, generally span only 1000–1600 m (600 m relief). Contours depict a subtle pattern of elevations increasing slightly from the northwestern and southeastern ends of the range toward the center of the range, and decreasing gradually to the northeast into the Mojave Desert. Much of the sinuosity of these contours likely results from pre-uplift topography, differential weathering and incision due to lithology, and minor amounts of post-uplift erosion. That the surface also contains many closed contours implies a heavy influence of inherited positive-relief forms associated with slow weathering and denudation, similar to the topography of the Mojave Desert. Contours were smoothed and redrafted at 200 m interval for Figure 13, depicting a much smoother, low-relief plateau. The long-wavelength slope of this plateau is ~3° to the northeast.

Although we used similar features to define and map it, the topography of the weathered surface in the SJM is quite different from that of the LSBM (Fig. 5A). In addition to consisting of more poorly defined polygons, the weathered surface covers a smaller fraction (about one-third) of the total mapped area of the SJM. As illustrated by the contour map (100 m interval), the surface also spans nearly 3× greater relief in the SJM (300–3100 m, or 2800 m relief) (Fig. 5B). Although contours are comparably sinuous and irregular in the SJM as in the LSBM, there are three distinct elevation zones in the SJM surface across which contours are difficult to connect. These include the main massif of the SJM (area 1), a lower mini-plateau that is separated by faults and slopes down to the Salton Trough (area 2), and a subordinate ridge to the southeast (area 3) that merges with the Santa Rosa Mountains (where the surface is absent) (Fig. 5A). The long-wavelength gradient of the surface in areas 1 and 3 averages ~9° and is locally as high as 15° down to the west-southwest, which is much steeper than in the LSBM (Fig. 4). This implies a very different vertical deformation field, pre-uplift topography, or post-uplift erosional modification of the erosion surface in the SJM relative to the LSBM.

Although areas 1 and 3 of the SJM are similar in form, they are difficult to connect through a pediment-capped 1800-m-high saddle, which also marks an abrupt bend in contour geometry from the north (N30°W) to the south (N70°W) (Fig. 13).

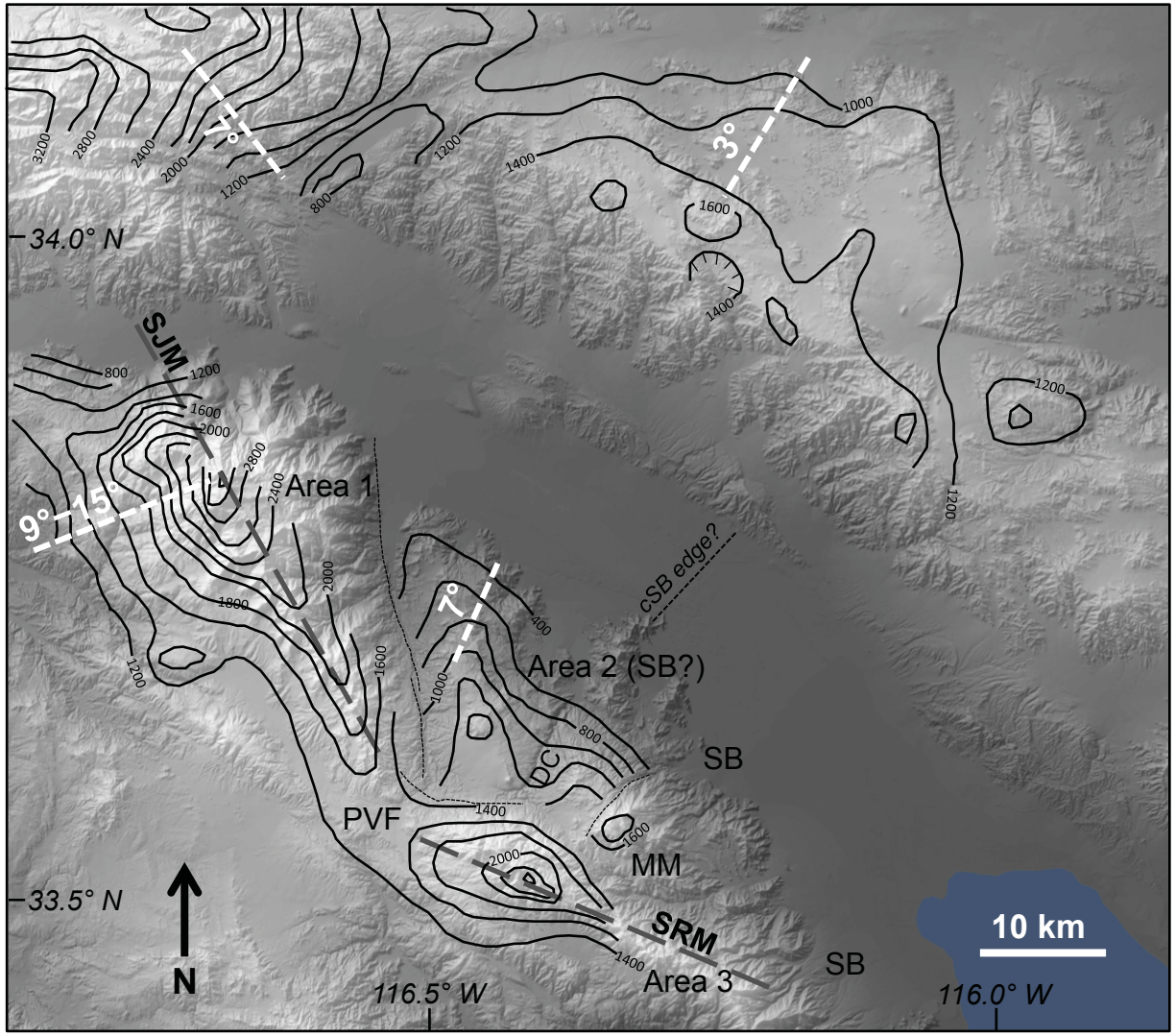

Figure 13. Structure contour map of the weathered erosion surface in the San Jacinto Mountains (SJM), Little San Bernardino Mountains, and southern San Bernardino Mountains. Contour interval is 200 m. Thick dashed gray line indicates the axes of the SJM and Santa Rosa Mountains (SRM), respectively. Thin dashed lines are selected faults (Rogers, 1965) that seem to disrupt contours. Dashed line labeled "cSB edge?" marks the proposed northern limit to the tilted central Salton block at about the location of Point Happy (location shown on Figure 14) as proposed by Dorsey and Langenheim (2015). Areas 1–3 are locations discussed in the text. White dashed lines illustrate directions along which mean surface gradients have been estimated (values shown). DC—Deep Canyon; MM—Martinez Mountain; PVF—Pinyon and Vandeventer flats; SB—Salton block (Dorsey and Langenheim, 2015).

This saddle lies between Pinyon and Vandeventer flats and contains the Pleistocene Bautista beds, which were sourced from the east and are now incised (Dorsey and Roering, 2006). These deposits indicate that the saddle is not due to recent erosion, that the SJM have been a sediment source throughout the Quaternary, and that stream flow must have wrapped around from the southeastern flank of the SJM to the southwest through this saddle prior to drainage reorganization associated with onset of motion on the San Jacinto fault zone (Dorsey and Roering, 2006).

DISCUSSION

Structural Interpretations of LSBM Uplift

The vertical distribution of erosion-surface remnants may provide clues to uplift mechanisms of the LSBM. The 200-m-contour map shown in Figure 13 includes the eastern Big Bear plateau and San Gorgonio blocks of the SBM to the northwest, which have been deformed as domal uplifts via displacement on underlying thrust faults (Spotila and Sieh, 2000). The resulting tilt associated with these convergent uplifts is ~7° (southeast). By comparison, the surface in the LSBM is of lower relief, tilting only ~3° northeast, and does not have the domal appearance that would be expected for uplift along a convergent structure. The northeast tilt is also lower than would be expected for a tilted normal-fault block. Footwall blocks of steep normal faults generally tilt away from bounding faults at 10°–25° for tens of kilometers (Stockli et al., 2003; Brown et al., 2017). AHe isochrons in the LSBM may locally tilt 8°, but only over a short distance (~2 km) (Fig. 12). The LSBM thus appear more like a flat, elevated table that simply drops off at the western escarpment, rather than a discrete block that has been deformed due to local uplift on an underlying or adjacent fault.

A potential explanation for uplift of the LSBM block with minimal local deformation is larger-scale flexural-isostatic uplift associated with crustal and mantle lithosphere thinning in the Coachella Valley and Salton Trough. In the flexural-isostatic model of Mueller et al. (2009) for the Sierra de San Pedro Mártir along the Gulf of California, for example, uplift magnitudes of 1–2 km are predicted across a zone ~150 km wide that is centered on the extensional zone. The corresponding tilts away from this welt are on the order of 1°–3°. We suggest that the LSBM have experienced broad isostatic uplift due to extension in the valley prior to onset of the present transpressional SAF regime. As such, the LSBM plateau may be best thought of as a gentle plateau with an asymmetric topographic divide that is now migrating backward away from the SAF. The broad, gentle uplift gradually tapers away to the northeast, such that the LSBM merges with the Mojave Desert ~30–40 km from the SAF. Based on Sabala's (2010) thermochronometry, the ca. 5 Ma onset of rapid exhumation associated with this broad uplift fits with extension in the Coachella Valley following activation of the West Salton detachment fault at 7–9 Ma (Shirvell et al., 2009; Dorsey et al., 2011; Mason et al., 2017), whereas uplift may have terminated in the past 1–2 m.y. with the onset of transpression (Matti and Morton, 1993; Powell, 1993; Janecke et al., 2010; Dorsey et al., 2011; Dorsey and Langenheim, 2015). This interpretation is broadly consistent with observations of topography and the LSBM range front. Subsequently, this broad zone of uplift could have been locally modified by faulting associated with the Eastern California shear zone (e.g., Blue Cut fault, or the north-trending faults of Hislop [2019]) and the SAF itself (e.g., local transpression as suggested by Sabala [2010]).

There are several alternative explanations for the uplift and topography of the LSBM. One possibility is that the broad uplift was produced or augmented by a crustal ramp along the SAF, which could have generated arching away from the surface trace of the SAF itself (Fuis et al., 2017). In this case, however, the zone of uplift might be expected to be more limited in width to the zone overlying the ramp. Another possibility is that the erosion surface and AHe isochrons originally dipped to the southwest, such that their moderate northeast tilt actually underestimates the magnitude of tectonic tilting associated with local faulting. A final alternative is that surface uplift and exhumation of the LSBM occurred due to a tectonic configuration that is no longer apparent. We note that at the time of rapid exhumation of the western escarpment (ca. 5 Ma), the LSBM were adjacent to the northern San Gabriel Mountains (between the Ridge Basin and Portal Ridge), which have since been translated 200 km along the SAF to the northwest (Dillon and Ehlig, 1993; Matti and Morton, 1993; Powell, 1993; Darin and Dorsey, 2013). The northern San Gabriel Mountains similarly exhibit a weathered erosion surface (e.g., Liebre Mountain) and young cooling ages that suggest onset of rapid exhumation at ca. 5 Ma (Buscher and Spotila, 2007). This exhumation has been interpreted to result from transpression and progressive stepping from the San Gabriel fault to the SAF via the Squaw Peak–Liebre Mountain thrust system (Buscher and Spotila, 2007). Although Sabala (2010) suggested that rapid cooling of the western LSBM has been ongoing since 5 Ma, models cannot rule out punctuated and short-lived exhumation. Given the similarity in cooling ages of blocks that were nearly adjacent at the time, it seems possible that uplift of these blocks was driven by a similar, but now inactive, tectonic driver.

Regardless of the structural mechanism, however, the preservation of the erosion surface and old AHe and AFT ages across most of the LSBM (i.e., east of the escarpment) limit the magnitude of denudation and rock uplift that could have occurred in the present tectonic regime. This shows that the LSBM have not been the site of major (i.e., more than a few kilometers of uplift), long-lived transpressive or transtensional deformation, unlike other ranges along the southern SAF system such as the San Bernardino and San Gabriel Mountains (Spotila et al., 1998; Blythe et al., 2000; Buscher and Spotila, 2007).

Structural Interpretations of SJM Uplift

The contour pattern in the erosion surface of the SJM suggests a different style of vertical deformation than in the LSBM. We interpret the lower, eastern segment of the range (area 2, Fig. 13), which is geographically a part of the Santa Rosa Mountains, to be a localized, low-amplitude rock

uplift associated with extension in the Salton Trough. This area exhibits erosion-surface contours with a long-wavelength gradient (~7° down to the northeast; Fig. 13) that is comparable to those of basement uplifts driven by convergent or extensional faulting (Spotila and Sieh, 2000; Stockli et al., 2003; Brown et al., 2017). The area is also incised (e.g., Deep Canyon; Fig. 13), suggesting recent base-level fall. We hypothesize that this area is an emergent pediment that may have been tilted down to the northeast as a part of the central Salton block defined by Dorsey and Langenheim (2015) farther to the south. The central Salton block has been suggested to have tilted down to the northeast 5°–10° in the last 1.2 m.y. due to convergence and loading across the northeast-dipping southern SAF (Fattaruso et al., 2014; Dorsey and Langenheim, 2015). Although Dorsey and Langenheim (2015) speculated that an unmapped tear fault near Point Happy (Fig. 13) bounds the northern margin of the tilted central Salton block, thereby separating it from area 2, we suggest that the similarity in tilt between these regions indicates that the zones are part of the same tilted basement block (Fig. 14). This interpretation would extend the central Salton block 20 km to the north. The central Salton block may also be faulted internally, such as at Martinez Mountain, a local topographic high that occurs just southeast of area 2 that may have been uplifted along a short, unnamed fault (Fig. 13) (Rogers, 1965). Likewise, the sharp rise from area 2 to area 1 (the SJM massif) may require local faulting, such as along the mapped but otherwise unstudied high-angle Palm Canyon fault (Fig. 14). The difference in appearance of area 2 (pediment) and versus the Salton block to the south (tilted valley fill) may reflect greater tilting or a shallower original basin geometry in the north. Local faults may also exist between area 2 and area 3, the Santa Rosa Mountains, although area 3 constitutes the western portion of the tilted central Salton block (Figs. 13, 14).

The uplift of the main SJM massif (area 1) is more difficult to explain. The steeply tilted, high erosion surface in area 1 is localized, isolated, and pinnacle-like, and does not obviously relate to local structures. Several lines of evidence also suggest that this massif was uplifted prior to the present tectonic configuration. The Pleistocene Bautista beds in Pinyon-Vandeventer flats (Fig. 13) and the evidence of an established rain shadow in Borrego Badlands lacustrine sediment suggest that the SJM may have already been high 1–2 m.y. ago (Cosma et al., 2002; Dorsey and Roering, 2006; Peryam et al., 2011). Thermochronometry also fails to demonstrate a Neogene or younger component of exhumation that could explain the present form of the SJM massif (Wolf et al., 1997; this study). We therefore consider it possible that the SJM massif was at least partially uplifted in a prior tectonic regime.

Farther south, the Peninsular Ranges batholith shares a similar long-wavelength, asymmetric topographic form as the SJM, with a steep eastern margin facing the Salton Trough and Gulf of California and a gently sloping western margin (Mueller et al., 2009; Seiler et al., 2011). Both regions display similar crustal thickness variations, from ~37 km on the west and thinning to ~27 km at the edge of the extensional region, thereby showing no evidence for an Airy root to isostatically support the topography (Lewis et al., 2000; Persaud et al., 2007). The topographic form of the Peninsular Ranges batholith in the south has been attributed to rift-shoulder uplift as a flexural-isostatic response to crustal thinning via normal faulting on the east and buoyancy associated with thinning or delamination of the mantle lithosphere, both as a result of transtensional plate motion since the late Miocene

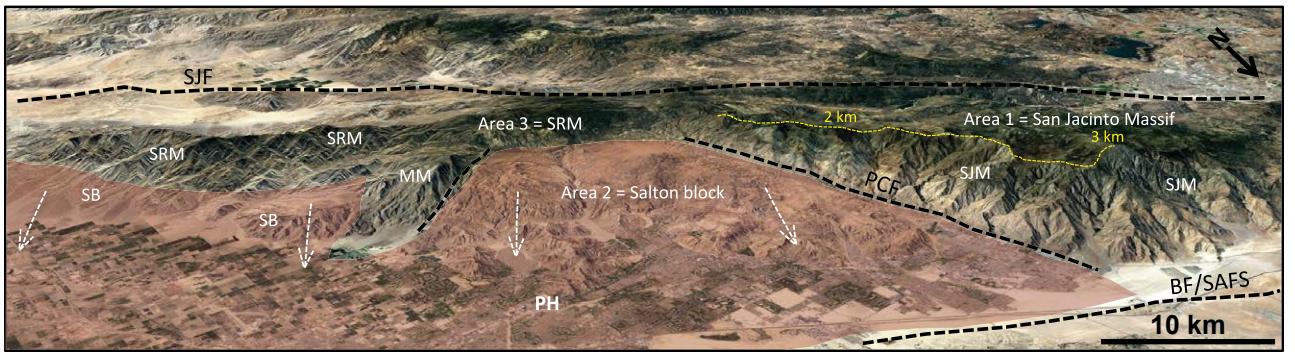

Figure 14. Three-dimensional perspective view of the proposed Salton block (SB). Red shading depicts the lower elevation of the block that forms the floor of Coachella Valley. The Santa Rosa Mountains (SRM), which are part of the block as defined by Dorsey and Langenheim (2015), are not shaded so as not to obscure their topographic relief. The northern limit of the central Salton block proposed by Dorsey and Langenheim (2015) is Point Happy (PH), but we propose that the block continues 20 km farther north to include all of our area 2. A small fault (dashed black line) may disrupt the surface and allow for local uplift of Martinez Mountain (MM) within the Salton block. This interpretation of the Salton block implies that the entire Santa Rosa Mountains (our area 3) are part of a continuous block that is structurally discontinuous with the San Jacinto Mountains (SJM) mass (area 1), perhaps separated by the Palm Canyon fault (PCF). Yellow line indicates how the massif rises from ~2 km to ~3 km elevation toward the north. BF/SAFS—Banning fault of San Andreas fault system; SJF—San Jacinto fault.

(Mueller et al., 2009; Seiler et al., 2011; Mark et al., 2014). The SJM massif may be a remnant of this rift shoulder (i.e., similar to the LSBM), which was subsequently modified by strike slip along the SAF and San Jacinto fault zone (Dorsey and Roering, 2006). The SJM may have also experienced rock uplift as the footwall of the West Salton detachment fault. Farther south in the Santa Rosa Mountains, Mason et al. (2017) estimated exhumation rates of 0.15–0.36 mm/yr due to footwall uplift. It is likely that the SJM experienced some degree of footwall uplift as well, given that the West Salton detachment fault occurs east of the range (Fig. 2).

A problem with likening the SJM massif to the rift shoulder developed elsewhere along the Salton Trough is its steep, pinnacle-like appearance. Unlike the Peninsular Ranges to the south or the broad uplift of the LSBM, the upper restored surface of the SJM massif does not exhibit a gentle tilt (Fig. 13). The western slope of the mapped erosion surface (9°–15°) is steeper than the gentle 1°–3° tilts expected for this rift shoulder elsewhere (Mueller et al., 2009; Mark et al., 2014). The height of the mapped surface in the SJM is also much higher than in the LSBM, and rises ~1.5 km along a north-northwest trend from the saddle with the Santa Rosa Mountains (Fig. 14). The northern and eastern escarpments of the SJM (Fig. 4), which are among the highest and steepest features of the entire plate boundary, are also steeper than generally expected for an older uplift. We hypothesize that this can be explained by erosional modification with or without local deformation from an undefined source.

A possible explanation for the height and ruggedness of the SJM massif is mechanical resistance to erosion. The granitic intrusions of the Peninsular Ranges batholith are known to be strong and coherent (Langenheim and Jachens, 2003; Langenheim et al., 2014). We hypothesize that the massif may have denuded more slowly than the surrounding region, and thus remained higher. The weathered erosion surface may have formed atop its rugged form with a nonhorizontal geometry. This would explain how the majority of the erosion surface tilts west, while the massif also exhibits east-dipping panels near San Jacinto Peak (Figs. 5, 9). This hypothesis suggests that ~1 km of the elevation of the SJM massif is relict and does not reflect Neogene rock uplift. The ruggedness of the SJM flanks may also be erosionally enhanced. DiBiase et al. (2018) suggested that the fracture spacing observed along the northern face may be ideal for holding up topography. Whereas a higher density of fractures in the San Gabriel Mountains translates to lower slopes and shorter cliffs, the spacing in the SJM may be low enough to preserve extremely steep faces, while also being high enough to prevent rounded, exfoliation-dominated hillslopes commonly observed in granitic terrain. We further suggest that contrasts in erodibility between lithologies may have contributed to the steep SJM flanks. The northern and eastern faces of the massif are surrounded by a perimeter of mylonite and gneiss (Figs. 4, 5A), which are heavily foliated and likely more erodible than the granitic core. Although these metamorphic units may be more chemically resistant and would be expected to form positive relief atop a deeply weathered granitic surface (as in the LSBM), their closer spacing of discontinuities may make them more susceptible to mechanical failure than the neighboring batholithic rocks. As the metamorphic rocks erode, they generate a rugged face that is partly reflective of the original structural contact between these lithologies. The degree to which erodibility explains the topography of the SJM requires additional testing, however.

Another possible explanation for the height and ruggedness of the SJM massif is local uplift associated with the convergent knot in the SAF at San Gorgonio Pass. Yule and Sieh (2003) suggested that impingement and loading against the SBM could cause down-to-the-north flexure of the SJM massif. Langenheim et al. (2005) also proposed wedging of the Peninsular Ranges under San Gorgonio Pass based on geophysical observations, including underthrusting in the shallow crust and possible uplift on a blind, south-dipping thrust that would push the SJM up and over strands of the SAF. These hypotheses for local deformation in San Gorgonio Pass fit with the observations of elevated seismicity, deep seismicity, and complex faulting in the pass. There is no structural or stratigraphic evidence of this deformation at the surface, however. In addition, boundary element modeling of the SAF system since reorganization and inception of the San Jacinto fault at 1.5 Ma does not indicate uplift in the area of the SJM (Cooke and Dair, 2011; Fattaruso et al., 2014, 2016), although these models do not specifically test the potential uplift due to blind thrusts. It therefore remains unknown whether the northward rise and ruggedness of the SJM massif is due to Neogene deformation or is a relict high that remains rugged due to erosional enhancement (or a combination of both).

CONCLUSIONS

Our observations quantify patterns of rock uplift in the eastern Transverse Ranges and northern Peninsular Ranges that can be integrated into tectonic understanding of the SAF system in the Coachella Valley. Data do not require either the LSBM or SJM to have been the locus of major (kilometer-scale) vertical deformation related to the SAF in the past few million years. Rapid exhumation after 5 Ma in the LSBM identified previously by Sabala (2010) may be the result of local SAF transpression, but can also be explained as rock uplift associated with an extensional rift shoulder. The latter interpretation suggests that the young ages represent the base of a tilted AHe PRZ, which is consistent with the broad tilting of a preserved erosion surface away from the Coachella Valley. Extensional uplift likely began after the 7–9 Ma onset of the West Salton detachment fault and possibly terminated after the SAF became transpressive a few million years ago.

We suggest that broad rift-shoulder uplift also affected the SJM, which similarly exhibit tilting away from the Coachella Valley and a lack of Neogene denudation from an erosion surface preserved at higher elevations. Although this uplift may have had similar timing as in the LSBM, evidence of this is not recorded in AHe ages, possibly due to a very low geothermal gradient (Wolf et al., 1997). Steeper tilt of the erosion surface in the SJM relative to the LSBM and the northward rise in the crest of the SJM may partly reflect vertical deformation associated with impingement of the northern Peninsular Ranges block into the SBM at San Gorgonio Pass,

but this is not currently quantifiable. Other geomorphic features of the SJM that have been previously suggested as evidence for recent convergent uplift do not actually require it. The ruggedness of the northern and western escarpments may in part reflect erosional resistance of the Peninsular Ranges batholith relative to the foliated metamorphic rock that wraps around its perimeter. The character of the range front below the rugged escarpment is consistent with burial of a formerly active normal fault. Evidence for topographic disequilibrium based on stream profile analysis (including distribution of normalized steepness index, k_{sn}) may also be explained by piecemeal capture and drainage-divide migration away from the Coachella Valley.

Although a fraction of SJM relief may thus be due to modern shortening, we instead propose that the SJM massif is a relict high formed by an earlier tectonic configuration. This hypothesis implies that one of the most striking mountain landforms along the entire plate boundary in California may actually be a fossil uplift. While this seems to be the simplest explanation, several key gaps in understanding remain. First, the timing of rock uplift remains unconstrained by thermochronology. Second, the kinematic effects of convergence along the SAF in San Gorgonio Pass on the northern SJM remain unknown. We suggest that until these problems are solved, the long-term kinematic evolution of fault systems through San Gorgonio Pass will remain incompletely understood.

Other portions of the northern Peninsular Ranges may be experiencing vertical deformation in the present tectonic configuration. This includes an emergent pediment to the north of Martinez Mountain, which we propose is the northward continuation of the eastward-tilting Salton block (Dorsey and Langenheim, 2015). Similarly, the area south of Pinyon-Vandeventer flats (area 3, Fig. 5A) appears to be part of the Santa Rosa Mountains, which has experienced uplift in the past 1–2 m.y. due to extension associated with the San Jacinto fault.

Regional preservation of the weathered granitic erosion surface is itself an important finding, which indicates that the SJM and LSBM have not been significant sources of sediment to basins outside of the Coachella Valley catchment. Significant sediment has been produced along the escarpments facing the valley in both ranges, however, as the Coachella Valley catchment has been enlarged via escarpment retreat.

These results are broadly consistent with kinematic models (Cooke and Dair, 2011; Fattaruso et al., 2014, 2016) that suggest that the LSBM and SJM have not been zones of major convergent uplift in the present tectonic configuration, despite their impressive topography. This indicates that topography is not always a simple indicator of vertical deformation, but instead may consist of an inherited, compound record that partly reflects earlier tectonics.

ACKNOWLEDGMENTS

Support for this study was provided by U.S. National Science Foundation (Tectonics Program) grants EAR-1145115 and EAR-1802026. Careful reviews from Julie Fosdick and Victoria Langenheim significantly improved the scientific content and style of this manuscript. The authors thank Rebecca Dorsey for scientific leadership and insight on this project, and Luke Sabala at Joshua Tree National Park for his prior work and sharing analytical data and insights from his M.S. thesis under the guidance of Phil Armstrong. Doug Yule and Michelle Cooke are thanked for organizing this special volume on San Gorgonio Pass.

REFERENCES CITED

Ague, J.J., and Brandon, M.T., 1992, Tilt and northward offset of Cordilleran batholiths resolved using igneous barometry: Nature, v. 360, p. 146–149, https://doi.org/10.1038/360146a0.

Ajala, R., Persaud, P., Stock, J.M., Fuis, G.S., Hole, J.A., Goldman, M., and Scheirer, D., 2019, Three-dimensional basin and fault structure from a detailed seismic velocity model of Coachella Valley, southern California: Journal of Geophysical Research, v. 124, p. 4728–4750, https://doi.org/10.1029/2018JB016260.

Atwater, T., and Stock, J., 1998, Pacific–North America plate tectonics of the Neogene southwestern United States: An update: International Geology Review, v. 40, p. 375–402, https://doi.org/10.1080/00206819809465216.

Axen, G.J., and Fletcher, J.M., 1998, Late Miocene–Pleistocene extensional faulting, northern Gulf of California, Mexico, and Salton Trough: International Geology Review, v. 40, p. 217–244, https://doi.org/10.1080/00206819809465207.

Axen, G.J., Grove, M., Stockli, D., Lovera, O.M., Rothstein, D.A., Fletcher, J.M., Farley, K., and Abbott, P.L., 2000, Thermal evolution of Monte Blanco dome: Low-angle normal faulting during Gulf of California rifting and late Eocene denudation of the eastern Peninsular Ranges: Tectonics, v. 19, p. 197–212, https://doi.org/10.1029/1999TC001123.

Barton, M.D., and Hanson, R.B., 1989, Magmatism and the development of low-pressure metamorphic belts: Implications from the western United States and thermal modeling: Geological Society of America Bulletin, v. 101, p. 1051–1065, https://doi.org/10.1130/0016-7606(1989)101<1051:MATDOL>2.3.CO;2.

Behr, W.M., Rood, D.H., Fletcher, K.E., Guzman, N., Finkel, R., Hanks, T.C., Hudnut, K.W., Kendrick, K.J., Platt, J.P., Sharp, W.D., Weldon, R.J., and Yule, J.D., 2010, Uncertainties in slip-rate estimates for the Mission Creek strand of the southern San Andreas fault at Biskra Palms Oasis, southern California: Geological Society of America Bulletin, v. 122, p. 1360–1377, https://doi.org/10.1130/B30020.1.

Bennett, S.E.K., Oskin, M.E., and Iriondo, A., 2013, Transtensional rifting in the proto–Gulf of California near Bahía Kino, Sonora, México: Geological Society of America Bulletin, v. 125, p. 1752–1782, https://doi.org/10.1130/B30676.1.

Binnie, S.A., Phillips, W.M., Summerfield, M.A., Fifield, L.K., and Spotila, J.A., 2008, Patterns of denudation through time in the San Bernardino Mountains, California: Implications for early-stage orogenesis: Earth and Planetary Science Letters, v. 276, p. 62–72, https://doi.org/10.1016/j.epsl.2008.09.008.

Blythe, A.E., Burbank, D.W., Farley, K.A., and Fielding, E.J., 2000, Structural and topographic evolution of the central Transverse Ranges, California, from apatite fission track, (U-Th)/He and digital elevation model analysis: Basin Research, v. 12, p. 97–114, https://doi.org/10.1046/j.1365-2117.2000.00116.x.

Brady, R.J., Ducea, M.N., Kidder, S.B., and Saleeby, J.B., 2006, The distribution of radiogenic heat production as a function of depth in the Sierra Nevada Batholith, California: Lithos, v. 86, p. 229–244, https://doi.org/10.1016/j.lithos.2005.06.003.

Brown, S.J., Thigpen, J.R., Spotila, J.A., Krugh, W.C., Tranel, L.M., and Orme, D.A., 2017, Onset timing and slip history of the Teton fault, Wyoming: A multidisciplinary reevaluation: Tectonics, v. 36, p. 2669–2692, https://doi.org/10.1002/2016TC004462.

Bull, W.B., 2007, Tectonic Geomorphology of Mountains: A New Approach to Paleoseismology: Malden, Massachusetts, Blackwell Publishing, 315 p., https://doi.org/10.1002/9780470692318.

Buscher, J.T., and Spotila, J.A., 2007, Near-field response to transpression along the southern San Andreas fault, based on exhumation of the northern San Gabriel Mountains, southern California: Tectonics, v. 26, TC5004, https://doi.org/10.1029/2006TC002017.

Calvet, M., Gunnell, Y., and Farines, B., 2015, Flat-topped mountain ranges: Their global distribution and value for understanding the evolution of mountain topography: Geomorphology, v. 241, p. 255–291, https://doi.org/10.1016/j.geomorph.2015.04.015.

Carter, J.N., Luyendyk, B.P., and Terres, R.R., 1987, Neogene clockwise rotation of the eastern Transverse Ranges, California, suggested by paleomagnetic vectors: Geological Society of America Bulletin, v. 98, p. 199–206, https://doi.org/10.1130/0016-7606(1987)98<199:NCTROT>2.0.CO;2.

Cecil, M.R., Ducea, M.N., Reiners, P.W., and Chase, C.G., 2006, Cenozoic exhumation of the northern Sierra Nevada, California, from (U-Th)/He thermochronology: Geological Society of America Bulletin, v. 118, p. 1481–1488, https://doi.org/10.1130/B25876.1.

Cooke, M.L., and Dair, L.C., 2011, Simulating the recent evolution of the southern big bend of the San Andreas fault, southern California: Journal of Geophysical Research, v. 116, B04405, https://doi.org/10.1029/2010JB007835.

Cosma, T.N., Smith, A.J., and Palmer, D.F., 2002, Uplift of the Peninsular Ranges affects terrestrial climate record of enhanced tropical moisture in late Pliocene, Anza-Borrego Desert, California: Geological Society of America Abstracts with Programs, v. 34, no. 6, p. 45.

Crosby, B.T., and Whipple, K.X., 2006, Knickpoint initiation and distribution within fluvial networks: 236 waterfalls in the Waipaoa River, North Island, New Zealand: Geomorphology, v. 82, p. 16–38, https://doi.org/10.1016/j.geomorph.2005.08.023.

Darin, M.H., and Dorsey, R.J., 2013, Reconciling disparate estimates of total offset on the southern San Andreas fault: Geology, v. 41, p. 975–978, https://doi.org/10.1130/G34276.1.

DiBiase, R.A., Whipple, K.X., Heimsath, A.M., and Ouimet, W.B., 2010, Landscape form and millennial erosion rates in the San Gabriel Mountains, CA: Earth and Planetary Science Letters, v. 289, p. 134–144, https://doi.org/10.1016/j.epsl.2009.10.036.

DiBiase, R.A., Rossi, M.W., and Neely, A.B., 2018, Fracture density and grain size controls on the relief structure of bedrock landscapes: Geology, v. 46, p. 399–402, https://doi.org/10.1130/G40006.1.

Dibblee, T.W., Jr., 1975, Late Quaternary uplift of the San Bernardino Mountains on the San Andreas and related faults, *in* Crowell, J.C., ed., San Andreas Fault in Southern California: A Guide to San Andreas Fault from Mexico to Carrizo Plain: California Division of Mines and Geology Special Report 118, p. 127–135.

Dibblee, T.W., Jr., 1981, Geology of the San Jacinto Mountains and adjacent areas, *in* Brown, A.R., and Ruff, R.W., eds., Geology of the San Jacinto Mountains: Santa Ana, California, South Coast Geological Society Annual Field Trip Guidebook 9, p. 1–47.

Dibblee, T.W., Jr., 1982, Geology of the San Bernardino Mountains, southern California, *in* Fife, D.L., and Minch, J.A., eds., Geology and Mineral Wealth of the California Transverse Ranges: Mason Hill Volume: Santa Ana, California, South Coast Geological Society Annual Symposium and Guidebook 10, p. 149–169.

Dillon, J.T., and Ehlig, P.L., 1993, Displacement on the southern San Andreas fault, *in* Powell, R.E., Weldon, R.J., and Matti, J.C., eds., The San Andreas Fault System: Displacement, Palinspastic Reconstruction, and Geologic Evolution: Geological Society of America Memoir 178, p. 199–216, https://doi.org/10.1130/MEM178-p199.

Dohrenwend, J.C., and Parsons, A.J., 2009, Pediments in arid environments, *in* Parsons, A.J., and Abrahams, A.D., eds., Geomorphology of Desert Environments (second edition): Dordrecht, Netherlands, Springer Science and Business Media, p. 377–411, https://doi.org/10.1007/978-1-4020-5719-9_13.

Dokka, R.K., 1984, Fission-track geochronologic evidence for Late Cretaceous mylonitization and early Paleocene uplift of the northeastern Peninsular Ranges, California: Geophysical Research Letters, v. 11, p. 46–49, https://doi.org/10.1029/GL011i001p00046.

Dorsey, R.J., and Langenheim, V.E., 2015, Crustal-scale tilting of the central Salton block, southern California: Geosphere, v. 11, p. 1365–1383, https://doi.org/10.1130/GES01167.1.

Dorsey, R.J., and Roering, J.J., 2006, Quaternary landscape evolution in the San Jacinto fault zone, Peninsular Ranges of Southern California: Transient response to strike-slip fault initiation: Geomorphology, v. 73, p. 16–32, https://doi.org/10.1016/j.geomorph.2005.06.013.

Dorsey, R.J., Housen, B.A., Janecke, S.U., Fanning, C.M., and Spears, A.L.F., 2011, Stratigraphic record of basin development within the San Andreas fault system: Late Cenozoic Fish Creek–Vallecito basin, southern California: Geological Society of America Bulletin, v. 123, p. 771–793, https://doi.org/10.1130/B30168.1.

Ehlers, T.A., and Farley, K.A., 2003, Apatite (U-Th)/He thermochronometry: Methods and applications to problems in tectonic and surface processes: Earth and Planetary Science Letters, v. 206, p. 1–14, https://doi.org/10.1016/S0012-821X(02)01069-5.

Farley, K.A., and Stockli, D.F., 2002, (U-Th)/He dating of phosphates: Apatite, monazite, and xenotime, *in* Kohn, M.J., Rakovan, J., and Hughes, J.M., eds., Phosphates: Geochemical, Geobiological, and Materials Importance: Reviews in Mineralogy and Geochemistry, v. 48, p. 559–578, https://doi.org/10.1515/9781501509636-018.

Farley, K.A., Wolf, R.A., and Silver, L.T., 1996, The effects of long alpha-stopping distances on (U-Th)/He dates: Geochimica et Cosmochimica Acta, v. 60, p. 4223–4229, https://doi.org/10.1016/S0016-7037(96)00193-7.

Fattaruso, L.A., Cooke, M.L., and Dorsey, R.J., 2014, Sensitivity of uplift patterns to dip of the San Andreas fault in the Coachella Valley, California: Geosphere, v. 10, p. 1235–1246, https://doi.org/10.1130/GES01050.1.

Fattaruso, L.A., Cooke, M.L., Dorsey, R.J., and Housen, B.A., 2016, Response of deformation patterns to reorganization of the southern San Andreas fault since ca. 1.5 Ma: Tectonophysics, v. 693, p. 474–488, https://doi.org/10.1016/j.tecto.2016.05.035.

Flint, J.J., 1974, Stream gradient as a function of order, magnitude, and discharge: Water Resources Research, v. 10, p. 969–973, https://doi.org/10.1029/WR010i005p00969.

Fosdick, J.C., and Blisniuk, K., 2018, Sedimentary signals of recent faulting along an old strand of the San Andreas fault, USA: Scientific Reports, v. 8, 12132, https://doi.org/10.1038/s41598-018-30622-3.

Fuis, G.S., Bauer, K., Goldman, M.R., Ryberg, T., Langenheim, V.E., Scheirer, D.S., Rymer, M.J., Stock, J.M., Hole, J.A., Catching, R.D., Graves, R.W., and Aagaard, B., 2017, Subsurface geometry of the San Andreas fault in Southern California: Results from the Salton Seismic Imaging Project (SSIP) and strong ground motion expectations: Bulletin of the Seismological Society of America, v. 107, p. 1642–1662, https://doi.org/10.1785/0120160309.

George, P.G., and Dokka, R.K., 1994, Major Late Cretaceous cooling events in the eastern Peninsular Ranges, California, and their implications for Cordilleran tectonics: Geological Society of America Bulletin, v. 106, p. 903–914, https://doi.org/10.1130/0016-7606(1994)106<0903:MLCCEI>2.3.CO;2.

Gold, P.O., Behr, W., Rood, D., Sharp, W., Rockwell, T., Kendrick, K., and Salin, A., 2015, Holocene geologic slip rate for the Banning strand of the southern San Andreas fault, southern California: Journal of Geophysical Research: Solid Earth, v. 120, p. 5639–5663, https://doi.org/10.1002/2015JB012004.

Gray, H.J., Shobe, C.M., Hobley, D.E.J., Tucker, G.E., Duvall, A.R., Harbert, S.A., and Owen, L.A., 2018, Off-fault deformation rate along the southern San Andreas fault at Mecca Hills, southern California, inferred from landscape modeling of curved drainages: Geology, v. 46, p. 59–62, https://doi.org/10.1130/G39820.1.

Hack, J.T., 1957, Studies of longitudinal stream profiles in Virginia and Maryland: U.S. Geological Survey Professional Paper 249-B, p. 45–97, https://doi.org/10.3133/pp294B.

Hislop, A., 2019, Fault evolution in the northwest Little San Bernardino Mountains, southern California: A reflection of tectonic linkage between the San Andreas fault and the Eastern California shear zone [Ph.D. thesis]: Lexington, University of Kentucky, 179 p., https://doi.org/10.13023/etd.2019.031.

House, M.A., Wernicke, B.P., Farley, K.A., and Dumitru, T.A., 1997, Cenozoic thermal evolution of the central Sierra Nevada, California, from (U-Th)/He thermochronometry: Earth and Planetary Science Letters, v. 151, p. 167–179, https://doi.org/10.1016/S0012-821X(97)81846-8.

Howard, A.D., and Kerby, G., 1983, Channel changes in badlands: Geological Society of America Bulletin, v. 94, p. 739–752, https://doi.org/10.1130/0016-7606(1983)94<739:CCIB>2.0.CO;2.

Janecke, S.U., Dorsey, R.J., Forand, D., Steely, A.N., Kirby, S.M., Lutz, A.T., Housen, B.A., Belgarde, B., Langenheim, V.E., and Rittenour, T.M., 2010, High Geologic Slip Rates since Early Pleistocene Initiation of the San Jacinto and San Felipe Fault Zones in the San Andreas Fault System: Southern California, USA: Geological Society of America Special Paper 475, 48 p., https://doi.org/10.1130/2010.2475.

Kirby, E., and Whipple, K., 2001, Quantifying differential rock-uplift rates via stream profile analysis: Geology, v. 29, p. 415–418, https://doi.org/10.1130/0091-7613(2001)029<0415:QDRURV>2.0.CO;2.

Kirby, E., Johnson, C., Furlong, K., and Heimsath, A., 2007, Transient channel incision along Bolinas Ridge, California: Evidence for differential rock uplift adjacent to the San Andreas fault: Journal of Geophysical Research, v. 112, F03S07, https://doi.org/10.1029/2006JF000559.

Langenheim, V.E., and Jachens, R.C., 2003, Crustal structure of the Peninsular Ranges batholith from magnetic data: Implications for Gulf of California rifting: Geophysical Research Letters, v. 30, 1597, https://doi.org/10.1029/2003GL017159.

Langenheim, V.E., and Powell, R.E., 2009, Basin geometry and cumulative offsets in the Eastern Transverse Ranges, southern California: Implications for transrotational deformation along the San Andreas fault system: Geosphere, v. 5, p. 1–22, https://doi.org/10.1130/GES00177.1.

Langenheim, V.E., Jachens, R.C., Matti, J.C., Hauksson, E., Morton, D.M., and Christensen, A., 2005, Geophysical evidence for wedging in the San Gorgonio Pass structural knot, southern San Andreas fault zone, southern California: Geological Society of America Bulletin, v. 117, p. 1554–1572, https://doi.org/10.1130/B25760.1.

Langenheim, V.E., Jachens, R.C., and Aiken, C., 2014, Geophysical framework of the Peninsular Ranges batholith—Implications for tectonic evolution and neotectonics, *in* Morton, D.M., and Miller, F.K., eds., Peninsular Ranges Batholith, Baja California and Southern California: Geological Society of America Memoir 211, p. 1–20, https://doi.org/10.1130/2014.1211(01).

Lewis, J.L., Day, S.M., Magistrale, H., Eakins, J., and Vernon, F., 2000, Regional crustal thickness variations of the Peninsular Ranges, southern California: Geology, v. 28, p. 303–306, https://doi.org/10.1130/0091-7613(2000)28<303:RCTVOT>2.0.CO;2.

Mark, C., Gupta, S., Carter, A., Mark, D., Gautheron, C., and Martin, A., 2014, Rift flank uplift at the Gulf of California: No requirement for asthenospheric upwelling: Geology, v. 42, p. 259–262, https://doi.org/10.1130/G35073.1.

Mason, C.C., Spotila, J.A., Axen, G., Dorsey, R.J., Luther, A., and Stockli, D.F., 2017, Two-phase exhumation of the Santa Rosa Mountains: Low- and high-angle normal faulting during initiation and evolution of the southern San Andreas fault: Tectonics, v. 36, p. 2863–2881, https://doi.org/10.1002/2017TC004498.

Matti, J.C., and Morton, D.M., 1993, Paleogeographic evolution of the San Andreas fault in southern California: A reconstruction based on a new cross-fault correlation, *in* Powell, R.E., Weldon, R.J., II, and Matti, J.C., eds., The San Andreas Fault System: Displacement, Palinspastic Reconstruction, and Geologic Evolution: Geological Society of America Memoir 178, p. 107–160, https://doi.org/10.1130/MEM178-p107.

Miggins, D.P., Premo, W.R., Snee, L.W., Yeoman, R., Naeser, N.D., Naeser, C.W., and Morton, D.M., 2014, Thermochronology of Cretaceous batholithic rocks in the northern Peninsular Ranges batholith, southern California: Implications for the Late Cretaceous tectonic evolution of southern California, *in* Morton, D.M., and Miller, F.K., eds., Peninsular Ranges Batholith, Baja California and Southern California: Geological Society of America Memoir 211, p. 199–261, https://doi.org/10.1130/2014.1211(06).

Miller, F.K., and Morton, D.M., 1980, Potassium-argon geochronology of the eastern Transverse Ranges and southern Mojave Desert, southern California: U.S. Geological Survey Professional Paper 1152, 30 p., https://doi.org/10.3133/pp1152.

Minch, J.A., 1979, The late Mesozoic–early Tertiary framework of continental sedimentation, northern Peninsular Ranges, Baja California, Mexico, *in* Abbott, P.L., ed., Eocene Depositional Systems, San Diego, California: Los Angeles, Society of Economic Paleontologists and Mineralogists, Pacific Section, p. 43–67.

Moser, A.C., Evans, J.P., Ault, A.K., Janecke, S.U., and Bradbury, K.K., 2017, (U-Th)/He thermochronometry reveals Pleistocene punctuated deformation and synkinematic hematite mineralization in the Mecca Hills, southernmost San Andreas fault zone: Earth and Planetary Science Letters, v. 476, p. 87–99, https://doi.org/10.1016/j.epsl.2017.07.039.

Mueller, K., Kier, G., Rockwell, T., and Jones, C.H., 2009, Quaternary rift flank uplift of the Peninsular Ranges in Baja and southern California by removal of mantle lithosphere: Tectonics, v. 28, TC5003, https://doi.org/10.1029/2007TC002227.

Muller, J., Lackey, J.S., Jicha, B., Hazlett, R.W., and Bindeman, I.N., 2014, Age and origin of the Malapai Hill basalt, Joshua Tree National Park, California: Geological Society of America Abstracts with Programs, v. 46, no. 5, p. 9.

Needy, S.K., Anderson, J.L., Wooden, J.L., Fleck, R.J., Barth, A.P., Paterson, S.R., Memeti, V., and Pignotta, G.S., 2009, Mesozoic magmatism in an upper- to middle-crustal section through the Cordilleran continental margin arc, eastern Transverse Ranges, California, *in* Miller, R.B., and Snoke, A.W., eds., Crustal Cross Sections from the Western North American Cordillera and Elsewhere: Implications for Tectonic and Petrologic Processes: Geological Society of America Special Paper 456, p. 187–218, https://doi.org/10.1130/2009.2456(07).

Nichols, K.K., Bierman, P.R., Hooke, R.L., Clapp, E.M., and Caffee, M., 2002, Quantifying sediment transport on desert piedmonts using ^{10}Be and ^{26}Al: Geomorphology, v. 45, p. 105–125, https://doi.org/10.1016/S0169-555X(01)00192-1.

Nichols, K.K., Bierman, P.R., Eppes, M.C., Caffee, M., Finkel, R., and Larsen, J., 2005, Late Quaternary history of the Chemehuevi Mountain piedmont, Mojave Desert, deciphered using ^{10}Be and ^{26}Al: American Journal of Science, v. 305, p. 345–368, https://doi.org/10.2475/ajs.305.5.345.

Oberlander, T.M., 1972, Morphogenesis of granitic boulder slopes in the Mojave Desert, California: The Journal of Geology, v. 80, p. 1–20, https://doi.org/10.1086/627710.

Oberlander, T.M., 1974, Landscape inheritance and the pediment problem in the Mojave Desert of southern California: American Journal of Science, v. 274, p. 849–875, https://doi.org/10.2475/ajs.274.8.849.

Oskin, M., and Stock, J., 2003, Pacific–North America plate motion and opening of the Upper Delfín basin, northern Gulf of California, Mexico: Geological Society of America Bulletin, v. 115, p. 1173–1190, https://doi.org/10.1130/B25154.1.

Pelletier, J.D., 2010, How do pediments form?: A numerical modeling investigation with comparison to pediments in southern Arizona, USA: Geological Society of America Bulletin, v. 122, p. 1815–1829, https://doi.org/10.1130/B30128.1.

Persaud, P., Pérez-Campos, X., and Clayton, R.W., 2007, Crustal thickness variations in the margins of the Gulf of California from receiver functions: Geophysical Journal International, v. 170, p. 687–699, https://doi.org/10.1111/j.1365-246X.2007.03412.x.

Peryam, T.C., Dorsey, R.J., and Bindeman, I., 2011, Plio-Pleistocene climate change and timing of Peninsular Ranges uplift in southern California: Evidence from paleosols and stable isotopes in the Fish Creek–Vallecito basin: Palaeogeography, Palaeoclimatology, Palaeoecology, v. 305, p. 65–74, https://doi.org/10.1016/j.palaeo.2011.02.014.

Pike, R.J., and Wilson, S.E., 1971, Elevation-relief ratio, hypsometric integral, and geomorphic area-altitude analysis: Geological Society of America Bulletin, v. 82, p. 1079–1084, https://doi.org/10.1130/0016-7606(1971)82[1079:ERHIAG]2.0.CO;2.

Powell, R.E., 1993, Balanced palinspastic reconstruction of pre–late Cenozoic paleogeology, southern California, *in* Powell, R.E., Weldon, R.J., II, and Matti, J.C., eds., The San Andreas Fault System: Displacement, Palinspastic Reconstruction, and Geologic Evolution: Geological Society of America Memoir 178, p. 1–106, https://doi.org/10.1130/MEM178-p1.

Powell, R.E., 2002a, Geologic map and digital database of the Pinto Mountain 7.5 minute quadrangle, Riverside County, California: U.S. Geological Survey Open-File Report 02-491, scale 1:24,000, with 34 p. text, https://doi.org/10.3133/ofr02491.

Powell, R.E., 2002b, Geologic map and digital database of the San Bernardino Wash 7.5 minute quadrangle, Riverside County, California: U.S. Geological Survey Open-File Report 02-498, scale 1:24,000, with 28 p. text, https://doi.org/10.3133/ofr02498.

Rogers, T.H., 1965, Geologic map of California, Santa Ana sheet: Sacramento, California Division of Mines and Geology, scale 1:250,000.

Rossi, M.W., 2014, Hydroclimatic controls on erosional efficiency in mountain landscapes [Ph.D. thesis]: Tempe, Arizona State University, 226 p.

Rossi, M.W., Quigley, M.C., Fletcher, J.M., Whipple, K.X., Díaz-Torres, J.J., Seiler, C., Fifield, L.K., and Heimsath, A.M., 2017, Along-strike variation in catchment morphology and cosmogenic denudation rates reveal the pattern and history of footwall uplift, Main Gulf Escarpment, Baja California: Geological Society of America Bulletin, v. 129, p. 837–854, https://doi.org/10.1130/B31373.1.

Rothstein, D.A., and Manning, C.E., 2003, Geothermal gradients in continental magmatic arcs: Constraints from the eastern Peninsular Ranges batholith, Baja California, México, *in* Johnson, S.E., Paterson, S.R., Fletcher, J.M., Girty, G.H., Kimbrough, D.L., and Martín-Barajas, A., eds., Tectonic Evolution of Northwestern México and the Southwestern USA: Geological Society of America Special Paper 374, p. 337–354, https://doi.org/10.1130/0-8137-2374-4.337.

Sabala, L.C., 2010, Exhumation and deformation history of the Little San Bernardino Mountains in the restraining bend of the San Andreas fault, southern California [M.S. thesis]: Fullerton, California State University, Fullerton, 219 p.

Sadler, P.M., and Reeder, W.W., 1983, Upper Cenozoic, quartzite-bearing gravels of the San Bernardino Mountains, southern California: Recycling and mixing as a result of transpressional uplift, *in* Anderson, D.W., and Rymer, M.J., eds., Tectonics and Sedimentation along Faults of the San Andreas System: Los Angeles, California, Society of Economic Paleontologists and Mineralogists, Pacific Section, p. 45–57.

Sawka, W.N., and Chappell, B.W., 1988, Fractionation of uranium, thorium, and rare earth elements in a vertically zones granodiorite: Implications for heat production distributions in the Sierra Nevada batholith, California, U.S.A: Geochimica et Cosmochimica Acta, v. 52, p. 1131–1143, https://doi.org/10.1016/0016-7037(88)90267-0.

Seiler, C., Fletcher, J.M., Quigley, M.C., Gleadow, A.J.W., and Kohn, B.P., 2010, Neogene structural evolution of the Sierra San Felipe, Baja California: Evidence for proto-gulf transtension in the Gulf Extensional Province?: Tectonophysics, v. 488, p. 87–109, https://doi.org/10.1016/j.tecto.2009.09.026.

Seiler, C., Fletcher, J.M., Kohn, B.P., Gleadow, A.J.W., and Raza, A., 2011, Low-temperature thermochronology of northern Baja California, Mexico: Decoupled slip-exhumation gradients and delayed onset of oblique rifting across the Gulf of California: Tectonics, v. 30, TC3004, https://doi.org/10.1029/2009TC002649.

Shirvell, C.R., Stockli, D.F., Axen, G.J., and Grove, M., 2009, Miocene-Pliocene exhumation along the west Salton detachment fault, southern California, from (U-Th)/He thermochronometry of apatite and zircon: Tectonics, v. 28, TC2006, https://doi.org/10.1029/2007TC002172.

Shuster, D.L., Flowers, R.M., and Farley, K.A., 2006, The influence of natural radiation damage on helium diffusion kinetics in apatite: Earth and Planetary Science Letters, v. 249, p. 148–161, https://doi.org/10.1016/j.epsl.2006.07.028.

Sieh, K., Jones, L., Hauksson, E., Hudnut, K., Eberhart-Phillips, D., Heaton, T., Hough, S., Hutton, K., Kanamori, H., Lilje, A., Lindvall, S., McGill, S.F., Mori, J., Rubin, C., Spotila, J.A., Stock, J., Thio, H.K., Treiman, J., Wernicke, B., and Zachariasen, J., 1993, Near-field investigations of the Landers earthquake sequence, April to July 1992: Science, v. 260, p. 171–176, https://doi.org/10.1126/science.260.5105.171.

Silver, L.T., and Chappell, B.W., 1988, The Peninsular Ranges batholith: An insight into the evolution of the Cordilleran

batholiths of southwestern North America: Transactions of the Royal Society of Edinburgh: Earth Sciences, v. 79, p. 105–121, https://doi.org/10.1017/S0263593300014152.

Snyder, N.P., Whipple, K.X., Tucker, G.E., and Merritts, D.J., 2000, Landscape response to tectonic forcing: Digital elevation model analysis of stream profiles in the Mendocino triple junction region, northern California: Geological Society of America Bulletin, v. 112, p. 1250–1263, https://doi.org/10.1130/0016-7606(2000)112<1250:LRTTFD>2.0.CO;2.

Spinler, J.C., Bennett, R.A., Anderson, M.L., McGill, S.F., Hreinsdottir, S., and McCallister, A., 2010, Present-day strain accumulation and slip rates associated with southern San Andreas and eastern California shear zone faults: Journal of Geophysical Research, v. 115, B11407, https://doi.org/10.1029/2010JB007424.

Spotila, J.A., 1999, The neotectonics of the San Bernardino Mountains and adjacent San Andreas fault: A case study of uplift associated with strike-slip fault systems [Ph.D. thesis]: Pasadena, California Institute of Technology, 378 p.

Spotila, J.A., 2005, Applications of low-temperature thermochronometry to quantification of recent exhumation in mountain belts, *in* Reiners, P.W., and Ehlers, T.A., eds., Low-Temperature Thermochronometry: Techniques, Interpretations, and Applications: Reviews in Mineralogy and Geochemistry, v. 58, p. 449–466, https://doi.org/10.2138/rmg.2005.58.17.

Spotila, J.A., and Berger, A.L., 2010, Exhumation at orogenic indentor corners under long-term glacial conditions: Example of the St. Elias orogen, southern Alaska: Tectonophysics, v. 490, p. 241–256, https://doi.org/10.1016/j.tecto.2010.05.015.

Spotila, J.A., and Sieh, K., 2000, Architecture of transpressional thrust faulting in the San Bernardino Mountains, southern California, from deformation of a deeply weathered surface: Tectonics, v. 19, p. 589–615, https://doi.org/10.1029/1999TC001150.

Spotila, J.A., Farley, K.A., and Sieh, K., 1998, Uplift and erosion of the San Bernardino Mountains associated with transpression along the San Andreas fault, California, as constrained by radiogenic helium thermochronometry: Tectonics, v. 17, p. 360–378, https://doi.org/10.1029/98TC00378.

Spotila, J.A., Farley, K.A., Yule, J.D., and Reiners, P.W., 2001, Near-field transpressive deformation along the San Andreas fault zone in southern California, based on exhumation constrained by (U-Th)/He dating: Journal of Geophysical Research, v. 106, p. 30,909–30,922, https://doi.org/10.1029/2001JB000348.

Spotila, J.A., Niemi, N., Brady, R., House, M., Buscher, J., and Oskin, M., 2007, Long-term continental deformation associated with transpressive plate motion: The San Andreas fault: Geology, v. 35, p. 967–970, https://doi.org/10.1130/G23816A.1.

Stockli, D.F., Dumitru, T.A., McWilliams, M.O., and Farley, K.A., 2003, Cenozoic tectonic evolution of the White Mountains, California and Nevada: Geological Society of America Bulletin, v. 115, p. 788–816, https://doi.org/10.1130/0016-7606(2003)115<0788:CTEOTW>2.0.CO;2.

Strahler, A.N., 1952, Hypsometric (area-altitude) analysis of erosional topography: Geological Society of America Bulletin, v. 63, p. 1117–1142, https://doi.org/10.1130/0016-7606(1952)63[1117:HAAOET]2.0.CO;2.

Strudley, M.W., Murray, A.B., and Haff, P.K., 2006, Regolith thickness instability and the formation of tors in arid environments: Journal of Geophysical Research, v. 111, F03010, https://doi.org/10.1029/2005JF000405.

Thatcher, W., Savage, J.C., and Simpson, R.W., 2016, The Eastern California Shear Zone as the northward extension of the southern San Andreas fault: Journal of Geophysical Research: Solid Earth, v. 121, p. 2904–2914, https://doi.org/10.1002/2015JB012678.

Twidale, C.R., 1990, The origin and implications of some erosional landforms: The Journal of Geology, v. 98, p. 343–364, https://doi.org/10.1086/629409.

van der Woerd, J., Klinger, Y., Sieh, K., Tapponnier, P., Ryerson, F.J., and Mériaux, A.-S., 2006, Long-term slip rate of the southern San Andreas fault from ^{10}Be-^{26}Al surface exposure dating of an offset alluvial fan: Journal of Geophysical Research, v. 111, B04407, https://doi.org/10.1029/2004JB003559.

Wahrhaftig, C., 1965, Stepped topography of the southern Sierra Nevada, California: Geological Society of America Bulletin, v. 76, p. 1165–1190, https://doi.org/10.1130/0016-7606(1965)76[1165:STOTSS]2.0.CO;2.

Whipple, K., Wobus, C., Crosby, B., Kirby, E., and Sheehan, D., 2007, New tools for quantitative geomorphology: Extraction and interpretation of stream profiles from digital topographic data: Short course presented at Geological Society of America 2007 Annual Meeting, Denver, Colorado, 28–31 October, 26 p.

Whipple, K.X., and Tucker, G.E., 1999, Dynamics of the stream power river incision model: Implications for height limits of mountain ranges, landscape response timescales, and research needs: Journal of Geophysical Research, v. 104, p. 17,661–17,674, https://doi.org/10.1029/1999JB900120.

Wobus, C.W., Crosby, B.T., and Whipple, K.X., 2006, Hanging valleys in fluvial systems: Controls on occurrence and implications for landscape evolution: Journal of Geophysical Research, v. 111, F02017, https://doi.org/10.1029/2005JF000406.

Wolf, R.A., Farley, K.A., and Silver, L.T., 1997, Assessment of (U-Th)/He thermochronometry: The low-temperature history of the San Jacinto mountains: California Geology, v. 25, p. 65–68, https://doi.org/10.1130/0091-7613(1997)025<0065:AOUTHT>2.3.CO;2.

Wollenberg, H.A., and Smith, A.R., 1968, Radiogeologic studies in the central part of the Sierra Nevada batholith, California: Journal of Geophysical Research, v. 73, p. 1481–1495, https://doi.org/10.1029/JB073i004p01481.

Yule, D., and Sieh, K., 2003, Complexities of the San Andreas fault near San Gorgonio Pass: Implications for large earthquakes: Journal of Geophysical Research, v. 108, 2548, https://doi.org/10.1029/2001JB000451.